ALMA Survey of Orion Planck Galactic Cold Clumps (ALMASOP) : How Do Dense Core Properties Affect the Multiplicity of Protostars?

Luo, Qiu-yi

2022-06-01

Luo , Q , Liu , T , Tatematsu , K , Liu , S-Y , Li , P S , Di Francesco , J , Johnstone , D , Goldsmith , P F , Dutta , S , Hirano , N , Lee , C-F , Li , D , Kim , K-T , Lee , C W , Lee , J-E , Liu , X , Juvela , M , He , J , Qin , S-L , Liu , H-L , Eden , D , Kwon , W , Sahu , D , Li , S , Xu , F-W , Zhang , S-J , Hsu , S-Y , Bronfman , L , Sanhueza , P , Pelkonen , V-M , Zhou , J , Liu , R , Gu , Q , Wu , Y-F , Mai , X , Falgarone , E & Shen , Z-Q 2022 , ' ALMA Survey of Orion Planck Galactic Cold Clumps (ALMASOP) : How Do Dense Core Properties Affect the Multiplicity of Protostars? ' , Astrophysical Journal , vol. 931 , no. 2 , 158 . https://doi.org/10.3847/1538-4357/ac66d9

http://hdl.handle.net/10138/348148
https://doi.org/10.3847/1538-4357/ac66d9

The Astrophysical Journal, 931:158 (22pp), 2022 June 1 https://doi.org/10.3847/1538-4357/ac66d9

ALMA Survey of Orion Planck Galactic Cold Clumps (ALMASOP): How Do Dense Core Properties Affect the Multiplicity of Protostars?

Qiu-yi Luo (罗秋怡)[1,2], Tie Liu (刘铁)[1], Ken'ichi Tatematsu[3,4], Sheng-Yuan Liu[5], Pak Shing Li[6], James di Francesco[7,8], Doug Johnstone[7,8], Paul F. Goldsmith[9], Somnath Dutta[5], Naomi Hirano[5], Chin-Fei Lee[5], Di Li[10], Kee-Tae Kim[11,12], Chang Won Lee[11,12], Jeong-Eun Lee[13], Xun-chuan Liu[1], Mika Juvela[14], Jinhua He[15,16,17], Sheng-Li Qin[18], Hong-Li Liu[18], David Eden[19,20], Woojin Kwon[21,22], Dipen Sahu[5], Shanghuo Li[11], Feng-Wei Xu[23,24], Si-ju Zhang[24], Shih-Ying Hsu[5,25], Leonardo Bronfman[17], Patricio Sanhueza[4,26], Veli-Matti Pelkonen[27], Jian-wen Zhou[2,10], Rong Liu[2,10], Qi-lao Gu[1], Yue-fang Wu[23,24], Xiao-feng Mai[1], Edith Falgarone[28], and Zhi-Qiang Shen[1]

[1] Shanghai Astronomical Observatory, Chinese Academy of Sciences, 80 Nandan Road, Shanghai 200030, People's Republic of China; lqy@shao.ac.cn, liutie@shao.ac.cn
[2] School of Astronomy and Space Sciences, University of Chinese Academy of Sciences, No. 19A Yuquan Road, Beijing 100049, People's Republic of China
[3] Nobeyama Radio Observatory, National Astronomical Observatory of Japan, National Institutes of Natural Sciences, Nobeyama, Minamimaki, Minamisaku, Nagano 384-1305, Japan
[4] Department of Astronomical Science, The Graduate University for Advanced Studies, SOKENDAI, 2-21-1 Osawa, Mitaka, Tokyo 181-8588, Japan
[5] Academia Sinica Institute of Astronomy and Astrophysics, 11F AS/NTU Astronomy-Mathematics Building, No. 1, Section 4, Roosevelt Road, Taipei 10617, Taiwan, R.O.C.
[6] Astronomy Department, University of California, Berkeley, CA 94720-3411, USA
[7] NRC Herzberg Astronomy and Astrophysics, 5071 West Saanich Road, Victoria, BC, V9E 2E7, Canada
[8] Department of Physics and Astronomy, University of Victoria, 3800 Finnerty Road, Elliot Building, Victoria, BC, V8P 5C2, Canada
[9] Jet Propulsion Laboratory, California Institute of Technology, 4800 Oak Grove Drive, Pasadena, CA 91109, USA
[10] National Astronomical Observatories of China, Chinese Academy of Sciences, Beijing 100012, People's Republic of China
[11] Korea Astronomy and Space Science Institute, 776 Daedeokdae-ro, Yuseong-gu, Daejeon 34055, Republic of Korea
[12] University of Science and Technology, Korea (UST), 217 Gajeong-ro, Yuseong-gu, Daejeon 34113, Republic of Korea
[13] The School of Space Research, Kyung Hee University, 1732 Deogyeong-daero, Giheung-gu, Yongin-si, Gyeonggi-do, Republic of Korea
[14] Department of Physics, P.O. Box 64, FI-00014, University of Helsinki, Finland
[15] Yunnan Observatories, Chinese Academy of Sciences, 396 Yangfangwang, Guandu District, Kunming 650216, People's Republic of China
[16] Chinese Academy of Sciences South America Center for Astronomy, National Astronomical Observatories, CAS, Beijing 100101, People's Republic of China
[17] Departamento de Astronomía, Universidad de Chile, Las Condes, 7591245 Santiago, Chile
[18] Department of Astronomy, Yunnan University, Kunming 650091, People's Republic of China
[19] Astrophysics Research Institute, Liverpool John Moores University, IC2, Liverpool Science Park, 146 Brownlow Hill, Liverpool, L3 5RF, UK
[20] Armagh Observatory and Planetarium, College Hill, Armagh, BT61 9DB, UK
[21] Department of Earth Science Education, Seoul National University, 1 Gwanak-ro, Gwanak-gu, Seoul 08826, Republic of Korea
[22] SNU Astronomy Research Center, Seoul National University, 1 Gwanak-ro, Gwanak-gu, Seoul 08826, Republic of Korea
[23] Department of Astronomy, School of Physics, Peking University, Beijing 100871, People's Republic of China
[24] Kavli Institute for Astronomy and Astrophysics, Peking University, Haidian District, Beijing 100871, People's Republic of China
[25] National Taiwan University (NTU), No. 1, Section 4, Roosevelt Road, Taipei 10617, Taiwan (R.O.C.)
[26] National Astronomical Observatory of Japan, National Institutes of Natural Sciences, 2-21-1 Osawa, Mitaka, Tokyo 181-8588, Japan
[27] Institut de Ciències del Cosmos, Universitat de Barcelona, IEEC-UB, Martí i Franquès 1, E-08028 Barcelona, Spain
[28] LPENS, Ecole Normale Supérieure, Université PSL, CNRS, Sorbonne Université, Université de Paris, 75005 Paris, France
Received 2022 March 7; revised 2022 April 12; accepted 2022 April 12; published 2022 June 6

Abstract

During the transition phase from a prestellar to a protostellar cloud core, one or several protostars can form within a single gas core. The detailed physical processes of this transition, however, remain unclear. We present 1.3 mm dust continuum and molecular line observations with the Atacama Large Millimeter/submillimeter Array toward 43 protostellar cores in the Orion molecular cloud complex (λ Orionis, Orion B, and Orion A) with an angular resolution of $\sim$0.″35 ($\sim$140 au). In total, we detect 13 binary/multiple systems. We derive an overall multiplicity frequency (MF) of 28% $\pm$ 4% and a companion star fraction (CSF) of 51% $\pm$ 6%, over a separation range of 300–8900 au. The median separation of companions is about 2100 au. The occurrence of stellar multiplicity may depend on the physical characteristics of the dense cores. Notably, those containing binary/multiple systems tend to show a higher gas density and Mach number than cores forming single stars. The integral-shaped filament of the Orion A giant molecular cloud (GMC), which has the highest gas density and hosts high-mass star formation in its central region (the Orion Nebula cluster), shows the highest MF and CSF among the Orion GMCs. In contrast, the λ Orionis GMC has a lower MF and CSF than the Orion B and Orion A GMCs, indicating that feedback from H II regions may suppress the formation of multiple systems. We also find that the protostars comprising a binary/multiple system are usually at different evolutionary stages.

Key words: Star formation – (1569); Early stellar evolution – (434); Protostars – (1302); Low mass stars – (2050); Multiple stars – (1081); Dense interstellar clouds – (371); Interstellar medium (847)

1. Introduction

Molecular clouds exhibit hierarchical structures at different levels from large to small scales. Dense cores lie at the terminus, where stars are born through gravitational fragmentation (Heggie 1975; Cohen & Kuhi 1979; Shu et al. 1987; Bergin & Tafalla 2007; Kraus & Hillenbrand 2012; Duchêne & Kraus 2013; Reipurth et al. 2014). Isolated star formation has been investigated for decades (di Francesco et al. 2007). The formation of binary/multiple-star systems, however, has been not as well studied, though these systems are commonly seen in star associations and clusters (Kraus & Hillenbrand 2012; Reipurth et al. 2014; Lomax et al. 2015; Dutta et al. 2020; Lee et al. 2020).

Binary/multiple systems in the main sequence have been studied for decades. Indeed, star systems that have more than one star are as common as single-star systems in the Milky Way (Lippincott 1978; Marcy & Benitz 1989; Duquennoy & Mayor 1991; Connelley et al. 2009; Raghavan et al. 2010). Previous near-infrared observational studies have concentrated on the multiplicity statistics for young stellar objects (YSOs) (Duchêne et al. 2004, 2007; Haisch et al. 2004; Kraus & Hillenbrand 2007; Connelley et al. 2008; Kraus et al. 2011; Daemgen et al. 2015; Kounkel et al. 2016; Ma et al. 2019). The high occurrence rates of multiple YSO systems revealed in these studies imply that stellar multiplicity is determined in the star formation process. In these surveys, the fraction of stars having companions (companion star fraction (CSF)) ranges from $16\% \pm 4\%$ to $62\% \pm 14\%$, and the fraction of systems having multiple YSOs (multiplicity frequency (MF)) ranges from $18\% \pm 4\%$ to $\sim$75%. In the past 10 years, high-resolution interferometric observations with the Submillimeter Array, Very Large Array (VLA), and Atacama Large Millimeter/submillimeter Array (ALMA) of nearby clouds have systematically revealed the multiplicity of low-mass protostars in still earlier phases, notably the Class 0/I phase (Chen et al. 2013; Lee et al. 2015; Hatziminaoglou et al. 2018). These observations indicate that the CSF ranges from $\sim$71% to $91\% \pm 5\%$ while the MF ranges from 40% to 60% for young protostars with separations below 10,000 au. Recently, higher angular resolution ALMA and VLA observations by Tobin et al. (2022) revealed the multiplicity of Orion protostars that were previously identified in the Herschel Orion Protostar Survey (HOPS): the CSF is $44\% \pm 3\%$ and the MF is $30\% \pm 3\%$.

Although different theoretical models of binary/multiple systems at various evolutionary stages have been proposed, e.g., turbulent fragmentation (Fisher 2004; Goodwin et al. 2004) and disk fragmentation (Adams et al. 1989; Bonnell & Bate 1994), the most relevant scenario remains unclear. Nevertheless, some predictions can be tested. For example, turbulent fragmentation suggests a nonlinear gravitational collapse, resulting in wider-separation binary/multiple systems (above 1000 au). On the other hand, disk fragmentation caused by gravitational instability is more likely to generate closer (below 600 au) binary/multiple systems (Beichman et al. 1986; Raghavan et al. 2010; Reipurth et al. 2007; Cohen & Kuhi 1979; Reipurth et al. 2014).

In a multiplicity study of all known protostars (94) in the Perseus molecular cloud, Tobin et al. (2016) found a bimodal distribution of separation among binary/multiple systems, with peaks at $\sim$75 au and $\sim$3000 au. The bimodal distribution was recently confirmed by a more detailed analysis of protostar separations in the Orion and Perseus molecular clouds (Tobin et al. 2022). Based on these results, Tobin et al. (2022) suggest that multiples with small separations (<500 au) are likely produced by both disk fragmentation and turbulent fragmentation with migration, and those with wide separation ($>10^3$ au) result primarily from turbulent fragmentation. Lee et al. (2017) found a low-mass binary system in the earliest stages of formation with the rotation axes of its disks misaligned, suggesting that this binary system is likely formed due to turbulent fragmentation. This system, however, has small separation ($\sim$860 au), which has probably been decreased by the migration of the protostars (Lee et al. 2020). Further, Tobin et al. (2016) detected a close triple system that was likely formed out of a protostellar disk undergoing gravitational instability.

However, previous investigations have rarely addressed how the properties of the host dense cores affect stellar multiplicity, even though they may play an important role. In this work, we explore the relation between the physical characteristics of dense cores and the formation of single or multiple stellar systems. This paper is structured as follows: Section 2 introduces our sample, and Section 3 describes the observational data from the surveys we use in the paper. In Section 4, we report the results of multiplicity analysis in binary/multiple systems. Section 5 discusses the origin of multiplicity, environmental effects, and physical and chemical differences among member protostars. Section 6 provides a summary.

2. The Sample

The Planck survey detected 13,188 Planck Galactic cold clumps (PGCCs) across the whole sky that exhibit extremely low temperatures ($T \sim 14$ K) (Planck Collaboration et al. 2016). PGCCs are therefore excellent targets for studying the very initial conditions of star formation (Juvela et al. 2010; Planck Collaboration et al. 2011; Wu et al. 2012; Montillaud et al. 2015; Planck Collaboration et al. 2016; Liu et al. 2018; Eden et al. 2019; Xu et al. 2020, 2021).

In follow-up observations, the James Clerk Maxwell Telescope (JCMT) large program SCOPE observed $\sim$1300 PGCCs in the 850 μm continuum to study the early evolution of dense cores, which targets high-column-density ($>5 \times 10^{20}$ cm^{-2} for a 5′ beam of the Planck telescope) clumps (Liu et al. 2018; Eden et al. 2019). The SCOPE sample is important for statistically investigating evolution between the starless and protostellar star formation phases.

The Orion Molecular Cloud Complex is about 380–420 pc away from us, and it has been extensively studied with many observations (Kim et al. 2020; Sahu et al. 2021a). As a part of SCOPE, Yi et al. (2018) turned to the Orion giant molecular cloud (GMC) complex, and observed 58 PGCCs in the three GMCs (Orion A, Orion B, and λ Orionis) with the JCMT in the 850 μm continuum. Beyond those they included 38 other PGCCs for which archival 850 μm continuum data were available in the JCMT Science Archive. The sample of Yi et al. (2018) is complete for PGCCs with column densities higher

than 5×10^{20} cm^{-2} (for a 5′ beam of the Planck telescope) in the Orion GMCs. In total, 119 dense cores were identified from JCMT SCUBA-2 observations of these Orion PGCCs, forming a unique sample of cold cores at similar distances for further studies.

As a follow-up observation of these Orion PGCCs, the ALMA Survey of Orion Planck Galactic Cold Clumps (ALMASOP) subsequently observed 72 of the 119 dense Orion PGCCs at high resolution (∼140 au). This resolution is high enough to resolve close binary/multiple systems with separations of a few hundred astronomical units. These 72 cores are among the densest in these clouds and are arguably the closest to the onset of star formation (Dutta et al. 2020), i.e., those that have started to collapse or have already formed protostars. In previous work with ALMASOP data, we focused on the chemical evolution of hot corino sources (Hsu et al. 2020, 2022), the fragmentation of prestellar cores (Sahu et al. 2021b), and outflow jets (Dutta et al. 2020).

Dutta et al. (2020) presented the 1.3 mm continuum emission maps in ALMASOP observations and identified protostars in 43 cores. Multiple protostars were frequently seen within a single core, but the multiplicity of these protostellar systems was not discussed in Dutta et al. (2020). The present paper investigates binary/multiple systems in ALMASOP, and focuses on how dense core properties relate to the multiplicity of protostars. The major limitation of this work is that very close binary systems with separation $\leqslant$140 au are not resolvable due to the angular resolution limits of the ALMASOP observation.

3. Observations and Data

3.1. ALMA Observations

ALMASOP (project ID: 2018.1.00302.S; PI: Tie Liu) observed 72 extremely cold young dense cores in the Orion molecular clouds, including 23 starless core candidates and 49 protostellar core candidates, with ALMA Band 6 from 2018 October to 2019 January. The observations were performed in four spectral windows centered at 216.6, 218.9, 231.0, and 233.0 GHz each with a 1.875 GHz bandwidth, with a velocity resolution of ∼1.4 km s^{-1}. Three array configurations were used for the observations: 12 m C43-5 (TM1), 12 m C43-2 (TM2), and 7 m Atacama Compact Array (ACA). Additional details of the observations are presented in Dutta et al. (2020). Several molecular line transitions were observed: CO(J = 2–1), C^{18}O(J = 2–1), N_2D^+(J = 3–2), DCO^+(J = 3–2), DCN (J = 3–2), and SiO(J = 5–4). In this paper, we utilize the results from the 1.3 mm continuum and CO(J = 2–1) data.

The acquired visibilities were calibrated with the standard pipeline in CASA (McMullin et al. 2007). The 1.3 mm continuum images were generated using the TCLEAN task of CASA with a threshold of 3σ theoretical sensitivity in three sets of the continuum images with the ACA (beam size ∼5.″8) FWHM, the TM2+ACA (beam size ∼1.″2) FWHM combination, and the TM1+TM2+ACA (beam size ∼0.″35) FWHM combination. We applied the "hogbom" deconvolver, and Briggs weighting with a robust value of +0.5 to obtain high-resolution maps, which allow us to identify multiple components more precisely. The TM1+TM2+ACA combination provides the best resolution to distinguish multiple components. The typical sensitivity of 1.3 mm continuum emission ranges from 0.01 to 0.2 mJy beam^{-1} in the TM1+TM2+ACA data (Dutta et al. 2020). The corresponding 3σ mass sensitivity is better than 0.002 $M_\odot$, assuming a dust temperature of 25 K and a distance of 400 pc.

3.2. JCMT SCUBA-2 Observations

The natal cores of the ALMASOP sources were observed in the 850 μm continuum with JCMT/SCUBA-2, as a part of the JCMT legacy survey SCOPE, "SCUBA-2 Continuum Observations of Pre-protostellar Evolution" (project ID: M16AL003; PI: Tie Liu). The beam size of JCMT at 850 μm is about 14″. An analysis of the 850 μm continuum emission of these dense cores was presented in Yi et al. (2018). The dense core parameters including the sizes, masses, and H_2 mean densities derived by Yi et al. (2018) are listed in Tables 1 and 2. It is worth mentioning that we have updated these parameters following new distance measurements as used in Kim et al. (2020), which are 380 pc for λ Orionis, 390 pc and 430 pc for Orion A, and 390 pc and 420 pc for Orion B.

3.3. No:45m Observations

The ALMASOP sources were also observed in nine molecular lines (CCS(J_N = 8$_7$–7$_6$), CCS(J_N = 7$_6$–6$_5$), HC_3N(J = 9–8), N_2H^+(J = 1–0), DNC(J = 1–0), $HN^{13}C$(J = 1–0), N_2D^+(J = 1–0), c-C_3H_2($J_{K_aK_c}$ = 2$_{12}$–101), and NH_3(J,K) = (1,1)) toward the 850 μm intensity peak positions of the SCUBA-2 cores with the 45 m radio telescope at Nobeyama Radio Observatory (No:45m; project IDs: CG161004, LP177001; PI: K. Tatematsu) from 2015 December to 2019 May (Tatematsu et al. 2017; Kim et al. 2020; Tatematsu et al. 2021). The observations were conducted with the receiver TZ1, T70, and FOREST which are dual-polarization and two-sideband superconductor–insulator–superconductor receivers. The velocity resolution is 0.05–0.06 km s^{-1} for both TZ1 and T70, 0.1 km s^{-1} for FOREST, and 0.05 km s^{-1} for H22. The details of the No:45m observations are described in Kim et al. (2020). Among the observed molecular lines, the N_2H^+ line emission exhibits a spatial distribution similar to that of the SCUBA-2 850 μm dust continuum emission (Tatematsu et al. 2017, 2021). Therefore, we adopt the Mach number, system velocity, line width (FWHM) of N_2H^+(J = 1–0), dust temperature, and H_2 column density from Kim et al. (2020) for further analysis in this work, which are compiled in Table 1 and Table 2. In addition, there are 16 dense cores in ALMASOP that were also mapped in N_2H^+(J = 1–0) line emission (Tatematsu et al. 2017, 2021). We also present the N_2H^+(J = 1–0) maps for these cores in this work.

3.4. Infrared Data

We used the Spitzer Enhanced Imaging Products (SEIP) from the Spitzer Heritage Archive (Megeath et al. 2012) and Wide-field Infrared Survey Explorer (WISE) data (Wright et al. 2010) to help classify protostars distributed throughout the region of the cores. The SEIP includes data from the four channels of the IRAC instrument (3.6, 4.5, 5.8, and 8 μm) and the 24 μm channel of the MIPS instrument. The WISE data were also observed in 3.4, 4.6, 12, and 22 μm. In this paper, we mainly use the highest-resolution 3.6/4.5/8 μm data in the SEIP observations or the highest-resolution 3.4/4.6/12 μm data in the WISE observations.

Table 1
Physics and Chemical Properties of Binary/Multiple Systems

							N_2H^+							
Source	R.A. (J2000)	Decl.(J2000)	Size	T_d	$N(H_2)$ ($\times 10^{23}$ cm^{-2})	n_{H_2} ($\times 10^5$ cm^{-3})	V_{lsr} (km s^{-1})	ΔV_{HFS} (km s^{-1})	ΔV_{GA} (km s^{-1})	$\mathcal{M}$	$M_{enve+disk}$	M_{core}	CGF	L_{jeans}
	(h:m:s)	(d:m:s)	(pc)	(K)	cm^{-2})	cm^{-3})	s^{-1})	s^{-1})	s^{-1})		($M_\odot$)	($M_\odot$)		(au)
(1)	(2)	(3)	(4)	(5)	(6)	(7)	(8)	(9)	(10)	(11)	(12)	(13)	(14)	(15)
G196.92-10.37	05:44:29.56	+09:08:50.20	0.22	14.8 ± 0.4	1.8 ± 0.1	5.6 ± 0.1	11.68	0.84	1.02	1.5 ± 0.2	0.116 ± 0.034	5.69 ± 0.32	0.02	7000
G205.46-14.56M1[a]	05:46:08.06	−00:10:43.71	0.09	12.5 ± 0.9	8.7 ± 0.8	35.9 ± 1.7	9.99	0.73	1.18	1.4 ± 0.1	2.309 ± 0.96	6.36 ± 1.33	0.36	2500
G205.46-14.56M2[a]	05:46:07.89	−00:10:01.82	0.06	12.5 ± 0.9	5.5 ± 0.5	22.6 ± 1.5	10.05	0.88	1.26	1.7 ± 0.1	0.291 ± 0.063	1.83 ± 0.38	0.16	3200
G205.46-14.56S1	05:46:07.05	−00:13:37.78	0.13	12.5 ± 0.9	6.7 ± 0.6	27.4 ± 1.7	10.31	1.18	1.23	2.4 ± 0.1	0.542 ± 0.179	11.64 ± 2.18	0.04	2900
G206.93-16.61E2	05:41:37.31	−02:17:18.13	0.10	16.8 ± 5.3	4.5 ± 1.5	18.8 ± 2.4	9.76	0.60	0.58	1.0 ± 0.1	0.863 ± 0.195	4.08 ± 0.16	0.21	4000
G207.36-19.82N1	05:30:50.94	−04:10:35.60	0.06	11.9 ± 1.4	3.5 ± 0.5	5.7 ± 1.1	10.52	1.13	1.48	2.3 ± 0.1	0.124 ± 0.048	1.15 ± 0.46	0.10	6200
G208.68-19.20N2	05:35:20.45	−05:00:50.39	0.05	19.7 ± 3.8	11.6 ± 3.0	18.9 ± 3.6	11.14	0.44	0.67	0.6 ± 0.1	4.786 ± 2.046	2.27 ± 1.15		4400
G208.68-19.20N3	05:35:18.02	−05:00:20.70	0.05	19.7 ± 3.8	11.7 ± 2.5	18.9 ± 3.7	11.12	0.69	0.96	1.1 ± 0.1	0.607 ± 0.195	2.65 ± 1.50	0.23	4400
G208.68-19.20S	05:35:26.32	−05:03:54.39	0.09	19.7 ± 3.8	4.6 ± 1.0	7.6 ± 1.4	10.35	0.95	0.94	1.5 ± 0.1	0.464 ± 0.190	3.55 ± 1.03	0.13	6900
G209.55-19.68N1	05:35:08.90	−05:55:54.40	0.16	14.1 ± 4.0	0.4 ± 0.1	0.7 ± 0.1	7.20	0.84	1.30	1.6 ± 0.1	0.334 ± 0.087	0.75 ± 0.04	0.44	19300
G210.49-19.79W	05:36:18.86	−06:45:28.03	0.11	11.8 ± 2.7	11.3 ± 2.9	18.4 ± 0.2	9.01	0.60	0.77	1.2 ± 0.1	0.209 ± 0.086	6.62 ± 0.25	0.03	3400
G210.97-19.33S2	05:38:45.30	−07:01:04.41	0.07	12.8 ± 1.1	1.2 ± 0.3	2.0 ± 0.1			0.86		0.038 ± 0.012	0.37 ± 0.09	0.10	10900
G211.47-19.27N	05:39:57.18	−07:29:36.07	0.07	12.4 ± 1.1	4.1 ± 0.4	6.6 ± 0.3	3.99	0.52	0.97	1.0 ± 0.2	0.105 ± 0.035	1.54 ± 0.43	0.06	5900
G212.10-19.15N2	05:41:24.03	−07:53:47.51	0.12	10.8 ± 1.4	1.8 ± 0.3	2.9 ± 0.3	4.45	0.69	1.04	1.5 ± 0.1	0.048 ± 0.016	1.53 ± 0.72	0.03	8300

Notes. Column(1): ALMASOP core name. Note that the marked [a] is different from the JCMT dense core name and those marked with * are dense core detected only in the ALMASOP survey. (2)-(3): coordinates in equatorial system (J2000) from (Yi et al. 2018) and (Dutta et al. 2020). (4): Core size from Yi et al. (2018). (5): Dust temperature comes from Kounkel et al. (2017). (6): H_2 column density cited from Kim et al. (2020). (7): H_2 number density from Yi et al. (2018). (8)-(10): N_2H^+(J=1-0) of systemic velocity, FWHM, and FWHM inferred by Gaussian fitting from Kim et al. (2020). (11): Mach number cited from Kim et al. (2020). (12): Gas mass of envelope and disk from Dutta et al. (2020).

Table 2
Physics and Chemical Properties of Single Systems

Source	R.A.(J2000)	Decl.(J2000)	Size	T_d	$N(H_2)$	n_{H_2}	N_2H^+			$\mathcal{M}$	$M_{envelope+disk}$	M_{core}	CGF	L_{jeans}
							V_{lsr}	ΔV_{HFS}	ΔV_{GA}					
(1)	(h:m:s) (2)	(d:m:s) (3)	(pc) (4)	(K) (5)	($\times 10^{23}$ cm^{-2}) (6)	($\times 10^5$ cm^{-3}) (7)	(km s^{-1}) (8)	(km s^{-1}) (9)	(km s^{-1}) (10)	(11)	($M_\odot$) (12)	($M_\odot$) (13)	(14)	(au) (15)
G191.90-11.21S	05:31:31.73	+12:56:14.99	0.10	14.7 ± 4.1	0.7 ± 0.2	2.2 ± 0.5	10.53	0.41	0.38	0.7 ± 0.1	0.079 ± 0.034	0.93 ± 0.09	0.085	11100
G192.12-11.10	05:32:19.54	+12:49:40.19	0.12	13.3 ± 3.0	1.8 ± 0.4	5.4 ± 0.2	10.02	0.73	0.35	1.4 ± 0.2	0.340 ± 0.145	2.32 ± 0.33	0.147	6800
G192.32-11.88N	05:29:54.47	+12:16:56.00	0.06	17.3 ± 6.0	1.1 ± 0.4	3.4 ± 0.4	12.12	0.66	0.59	1.1 ± 0.2	0.408 ± 0.174	0.51 ± 0.05	0.800	9700
G192.32-11.88S	05:29:54.74	+12:16:32.00	0.05	17.3 ± 6.0	0.9 ± 0.4	2.9 ± 0.2	12.08	0.54	0.58	0.9 ± 0.1	0.100 ± 0.043	0.23 ± 0.02	0.435	10500
G200.34-10.97N	05:49:03.71	+05:57:55.74	0.09	13.5 ± 0.9	0.8 ± 0.1	2.5 ± 0.6	13.36	0.45	0.51	0.8 ± 0.1	0.068 ± 0.029	0.81 ± 0.06	0.084	10000
G201.52-11.08	05:50:59.01	+04:53:53.10	0.05	13.6 ± 1.3	0.8 ± 0.1	3.3 ± 0.8					0.060 ± 0.026	0.14 ± 0.04	0.429	8800
G203.21-11.20W1	05:53:42.83	+03:22:32.90	0.12	11.2 ± 0.7	2.7 ± 0.3	11.1 ± 1.9	10.70	0.50	1.02	1.0 ± 0.1	0.091 ± 0.039	2.88 ± 0.13	0.032	4300
G203.21-11.20W2	05:53:39.62	+03:22:24.90	0.10	11.2 ± 0.7	3.2 ± 0.4	13.4 ± 1.5	10.11	0.50	0.72	1.0 ± 0.1	0.034 ± 0.015	2.57 ± 0.19	0.013	3900
G205.46-14.56N1[a]	05:46:09.65	−00:12:16.45	0.05	12.5 ± 0.9	5.5 ± 0.5	22.5 ± 1.1	9.92		1.34		0.475 ± 0.203	1.06 ± 0.16	0.448	3200
G205.46-14.56N2[a]	05:46:07.49	−00:12:22.42	0.03	12.5 ± 0.9	4.7 ± 0.4	19.2 ± 1.9	10.29	0.70	0.75	1.4 ± 0.1	0.223 ± 0.095	0.49 ± 0.09	0.475	3500
G205.46-14.56S2	05:46:04.49	−00:14:18.87	0.03	12.5 ± 0.9	4.8 ± 0.5	19.8 ± 2.9	10.44	0.46	0.54	0.9 ± 0.1	0.069 ± 0.029	0.47 ± 0.10	0.147	3400
G205.46-14.56S3	05:46:03.54	−00:14:49.34	0.04	12.5 ± 0.9	5.0 ± 0.5	20.4 ± 1.9	10.36	0.61	0.81	1.2 ± 0.1	0.167 ± 0.072	0.88 ± 0.16	0.190	3300
G206.12-15.76	05:42:45.26	−01:16:11.37	0.14	11.9 ± 1.6	2.6 ± 0.4	10.8 ± 1.3					1.035 ± 0.442	3.95 ± 1.73	0.262	4500
G206.93-16.61W2[a]	05:41:25.04	−02:18:08.11	0.06	16.8 ± 5.3	9.9 ± 3.1	40.08 ± 4.7	9.25	0.65	1.02	1.1 ± 0.1	0.771 ± 0.333	3.27 ± 0.15	0.235	2800
G208.68-19.20N1	05:35:23.37	−05:01:28.70	0.09	19.7 ± 3.8	10.9 ± 2.4	17.7 ± 3.4	11.13	0.72	0.96	1.1 ± 0.1	2.312 ± 0.988	7.79 ± 2.53	0.297	4500
G208.68-20.04E	05:32:48.40	−05:34:47.14	0.13	12.8 ± 4.2	2.6 ± 0.9	4.3 ± 0.3	8.74	0.38	0.52	0.7 ± 0.1	0.073 ± 0.031	3.95 ± 0.29	0.018	7400
G208.89-20.04Walma[*]	05:32:28.03	−05:34:26.69									0.028 ± 0.012			
G209.55-19.68S1	05:35:13.25	−05:57:58.65	0.23	14.1 ± 4.0	0.8 ± 0.2	1.2 ± 0.2	7.35	0.68	0.94	1.3 ± 0.1	0.264 ± 0.113	2.31 ± 0.97	0.114	14800
G209.55-19.68S2[a]	05:35:08.96	−05:58:26.38	0.16	14.1 ± 4.0	1.0 ± 0.3	1.6 ± 0.5	8.11	0.45	0.51	0.8 ± 0.1	0.084 ± 0.036	1.52 ± 0.26	0.054	12800
G210.37-19.53S	05:37:00.55	−06:37:10.16	0.15	14.0 ± 4.1	1.1 ± 0.3	1.8 ± 0.7	5.61	0.72	0.69	1.3 ± 0.1	0.133 ± 0.050	2.27 ± 0.23	0.059	12000
G210.82-19.47S	05:38:03.67	−06:58:24.141	0.08		0.4 ± 0.1	0.7 ± 0.8					0.010 ± 0.004	0.22 ± 0.125	0.600	
G211.01-19.54N	05:37:57.23	−07:06:56.72	0.10	14.7 ± 8.4	2.5 ± 1.4	4.1 ± 0.2	6.03	0.83	0.79	1.5 ± 0.1	0.130 ± 0.056	2.16 ± 0.36	0.060	8200
G211.01-19.54S	05:37:59.04	−07:07:24.14	0.07	14.7 ± 8.4	2.5 ± 1.4	4.0 ± 0.1	5.72	0.70	1.01	1.3 ± 0.1	0.021 ± 0.009	1.05 ± 0.32	0.020	8300
G211.16-19.33N2	05:39:05.83	−07:10:41.52	0.10	12.5 ± 1.8	0.8 ± 0.1	1.2 ± 0.1	3.49	0.46	0.70	0.9 ± 0.1	0.016 ± 0.007	0.48 ± 0.20	0.033	13900
G211.47-19.27S	05:39:56.10	−07:30:28.40	0.01	12.4 ± 1.1	7.2 ± 0.8	11.7 ± 0.3	5.52	1.03	0.93	2.1 ± 0.1	0.990 ± 0.424	11.39 ± 3.18	0.087	4500
G212.10-19.15S	05:41:26.39	−07:56:51.81	0.15	10.8 ± 1.4	1.9 ± 0.3	3.0 ± 0.4	3.78	0.38	0.74	0.6 ± 0.1	0.237 ± 0.101	2.41 ± 1.00	0.098	8200
G212.84-19.45N	05:41:32.07	−08:40:10.94	0.10	11.7 ± 1.1	2.0 ± 0.2	3.2 ± 0.5	4.31	0.34	0.42	0.8 ± 0.1	0.273 ± 0.117	1.26 ± 0.50	0.217	8300
G215.87-17.62M	05:53:32.52	−10:25:05.99	0.24	12.2 ± 1.2	0.5 ± 0.1	0.8 ± 0.1	8.96	0.35	0.46	0.7 ± 0.1	0.065 ± 0.028	2.50 ± 0.64	0.026	16800
G215.87-17.62N	05:53:41.91	−10:24:02.00	0.26	12.2 ± 1.2	0.6 ± 0.1	1.0 ± 0.2	9.28	0.46	0.89	0.9 ± 0.4	0.0090 ± 004	3.96 ± 0.84	0.002	15000

Notes. Column(1): ALMASOP core name. Note that the marked [a] is different from the JCMT dense core name and those marked with * are dense core detected only in the ALMASOP survey. (2)-(3): coordinates in equatorial system (J2000) from (Yi et al. 2018) and Dutta et al. (2020). (4): Core size from Yi et al. (2018). (5): Dust temperature comes from Kounkel et al. (2017). (6): H_2 column density cited from Kim et al. (2020). (7): H_2 number density from Yi et al. (2018). (8)-(10): N_2H^+(J=1-0) of systemic velocity, FWHM, and FWHM inferred by Gaussian fitting from Kim et al. (2020). (11): Mach number cited from Kim et al. (2020). (12): Gas mass of envelope and disk from Dutta et al. (2020).

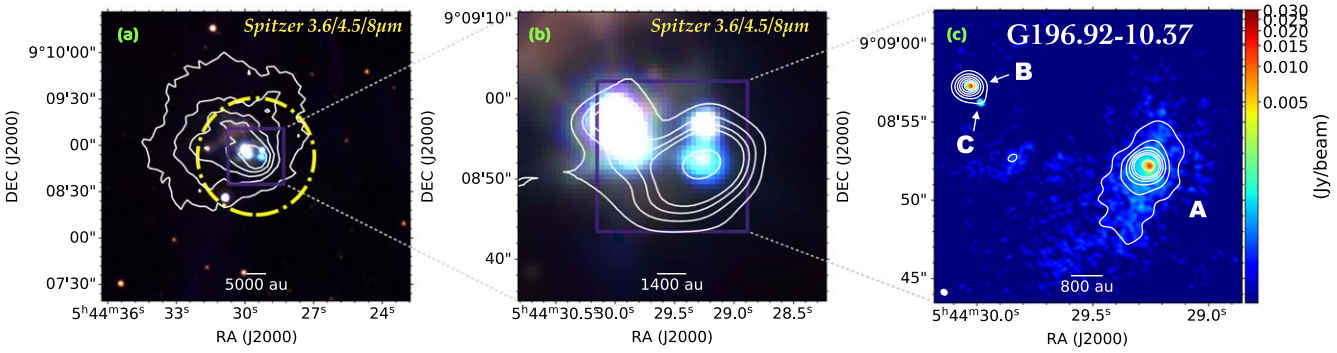

Figure 1. Images of an exemplar core G196.92-10.37. (a) JCMT SCUBA-2 850 μm contours superimposed with RGB image of Spitzer 3.6/4.5/8 μm data. The yellow circle represents the field of view (FOV) of the ALMA ACA image shown in panel (b). The contour levels are from 6σ to 30σ with steps of 6σ (1σ is 13.8 mJy beam^{-1}). (b) Zoom into the infrared data, with contours of the ALMA ACA 1.3 mm dust continuum data. The contour levels are 3σ, 6σ, 9σ, 12σ, and 30σ (1σ is 5 mJy beam^{-1}). (c) Color image showing ALMA 1.3 mm dust continuum emission from combined TM1+TM2+ACA data, and contours showing the 1.3 mm dust continuum emission from lower-resolution TM2+ACA data. The contours correspond to 5σ, 10σ, 15σ, 20σ, 25σ, 30σ, 50σ, 70σ, and 90σ (1σ is 4 mJy beam^{-1}).

4. Results

4.1. Identification of Binary/Multiple Systems

We focus on the 43 protostellar cores among 72 cores that were detected in 1.3 mm continuum emission in ALMASOP (Dutta et al. 2020). The 1.3 mm continuum emission from these cores is relatively bright, and indicates that one or more compact objects, previously identified as young protostars (Dutta et al. 2020), have formed within them. Figure 1 presents the infrared and (sub)millimeter continuum images obtained with various instruments for an exemplar core G196.92-10.37. Multiple point sources are seen in the Spitzer image but some may be contamination from background/foreground stars or very evolved protostars because they do not show strong 1.3 mm continuum emission (Tobin et al. 2022). We will only consider young protostars with disks and envelopes, which should have strong 1.3 mm continuum emission, in further multiplicity analysis. From the highest-resolution ALMA 1.3 mm continuum image shown in the right panel, one can identify a triple protostellar system formed in the exemplar core G196.92-10.37. The image descriptions of the other cores are compiled in Appendix.

We identify binary/multiple systems within the SCUBA-2 cores, whose sizes are smaller than or comparable to the FOV of the ALMA 12 m array, following the same strategy used in previous works (e.g., Tobin et al. 2016, 2022). The core sizes are listed in Tables 1 and 2. In total, we identify 13 binary/multiple systems and 29 single systems, and one binary-system candidate (one of its members is a prestellar core). Here we note again that our observations cannot resolve systems with below 140 au separation; thus some single-star systems could also be very close binary/multiple systems. Some ALMASOP sources were also observed in the VANDAM survey (see Table 6 in the Appendix; Tobin et al. 2022). We find that two single-protostar systems (G206.12-15.76 and G211.47-19.27S) in ALMASOP were further resolved to very close binary/multiple systems in the VANDAM survey. However, the very close binary/multiple systems in G206.12-15.76 and G211.47-19.27S are apparently formed due to disk fragmentation, and hence their properties are not determined by the fragmentation of their natal dense cores. Therefore, they are treated as single stars in the below analysis of the relations between core properties and protostellar multiplicity. The other single stars in ALMASOP remain to be single in the VANDAM survey.

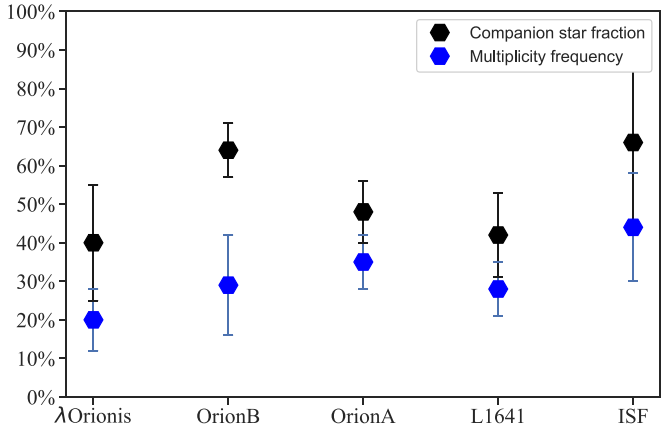

Figure 2. MF (blue hexagons) and CSF (black hexagons) in three GMCs (λ Orionis, Orion A, and Orion B) in the Orion region, and in two subregions of Orion A, L1641 and ISF.

To quantify the multiplicity in each Orion GMC, we adopt the statistical parameters of MF and CSF. They give a good indication of the proportion of binary/multiple systems and the average number of companions. The two quantities associated with the number of star systems and companions are given by

$$\mathrm{MF} = \frac{B + T + Q + \ldots}{S + B + T + Q \ldots} \quad (1)$$

$$\mathrm{CSF} = \frac{B + 2T + 3Q + \ldots}{S + B + T + Q \ldots} \quad (2)$$

where S, B, T, and Q are the numbers of single, binary, triple, and quadruple systems in the sample, respectively. Figure 2 shows the MF and CSF of each of the three Orion GMCs, and the actual quantities are listed in Table 3. As the two subregions (separated by a $-6°$ decl.) of Orion A, the integral-shaped filament (ISF) and L1641, have very different physical environments and levels of star formation activity (Megeath et al. 2016), we also calculate their MF and CSF separately. The overall MF and CSF for the ALMASOP sample are $28\% \pm 4\%$ and $51\% \pm 6\%$, respectively. For comparison, Tobin et al. (2022) found that the overall MF and CF for the HOPS protostars are $30\% \pm 3\%$ and $44\% \pm 3\%$, respectively, which are broadly consistent with our statistical results. However, we note that their sample contains very close

Table 3
Stellar Multiplicity in Orion Molecular Cloud Complex

Subregion	MF	CSF	Sample Number (Single Systems)	Sample Number (Binary Systems)	Sample Number (Triple Systems)	Sample Number (Quadruple Systems)	Sample Number (Five-star Systems)
(1)	(2)	(3)	(4)	(5)	(6)	(7)	(8)
λ Orionis	$20\% \pm 8\%$	$40\% \pm 15\%$	4	0	1	0	0
Orion B	$29\% \pm 7\%$	$64\% \pm 13\%$	10	2	0	1	1
Orion A	$35\% \pm 7\%$	$48\% \pm 8\%$	15	5	2	1	0
L1641	$28\% \pm 7\%$	$42\% \pm 11\%$	10	3	0	1	0
ISF	$44\% \pm 14\%$	$66\% \pm 22\%$	5	2	2	0	0

binary/multiple systems with separations smaller than 100 au, which cannot be resolved in our observations.

In our sample, the λ Orionis cloud shows the lowest MF and CSF, and the ISF region in Orion A shows the highest MF and CSF. When comparing the two subregions of Orion A, the ISF region, which contains the Orion Nebula cluster (ONC), has much higher multiplicity than L1641. The different occurrences of stellar multiplicity in the Orion GMCs may be caused by environmental effects such as stellar feedback, gas density, and turbulence levels, which we explore later in Section 5.

4.2. Properties of the Natal Dense Cores

We are interested in how the properties of dense cores affect the multiplicity of the protostars that form within them. To explore this possible connection, we summarize detailed information of the 43 protostellar cores from previous studies and divide the cores into two groups: dense cores forming single stars and dense cores forming more than one protostar. As the assumptions and calculation procedures for many of the parameters have already been described in detail in previous works (Yi et al. 2018; Kim et al. 2020; Dutta et al. 2020), we simply describe the core parameters here. The core parameters of these two groups are listed in Tables 1 and 2.

Yi et al. (2018) used the ClumpFind task in the STARLINK package to identify dense cores. The method was to fit the SCUBA-2 850 μm continuum emission maps in 2D Gaussian profiles with a threshold of 5σ. ClumpFind limited the edge of the core according to the threshold, and extracted the sizes and fluxes relying on the FWHM brightness and the integrated fluxes of the core.

The flux density produced by the SCUBA-2 850 μm dust emission can be expressed as

$$S_\nu^{'} = \Omega \tau_\lambda B_\nu(T_{\rm dust}) = \Omega \mu m_{\rm H} \kappa_\nu B_\nu(T_{\rm dust}). \quad (3)$$

The H_2 column density of the cores can therefore be derived from the flux density. The calculation of the following parameters, with flux density involved, follows the optically thin assumption:

$$N(H_2) = \frac{S_\nu^{'}}{\Omega \mu m_{\rm H} \kappa_\nu B_\nu(T_{\rm dust})} \quad (4)$$

where $S_\nu^{'}$ is the beam-averaged flux density, τ_λ is the dust optical depth, Ω is the solid angle of the source, μ is the mean molecular weight and its value is 2.8, $m_{\rm H}$ is the mass unit of atomic hydrogen, and $B_\nu(T_{\rm dust})$ is the Planck function of dust temperature $T_{\rm dust}$, which is from the PGCC catalog. The dust opacity per gram of gas is calculated following the equation from Beckwith et al. (1990): $\kappa_\nu = 0.1(\nu/10^{12}{\rm Hz})^\beta$ cm^2 g^{-1}, where β is the dust emissivity spectral index from Planck Collaboration et al. (2016). The column densities of the 43 protostellar cores in the ALMASOP sample range from $0.4 \pm 0.1 \times 10^{23}$ cm^{-2} to $11.7 \pm 2.5 \times 10^{23}$ cm^{-2}, with a median value of 2.5×10^{23} cm^{-2}.

The mean H_2 number densities of the cores are estimated from the H_2 column densities based on the SCUBA-2 850 μm dust continuum:

$$n_{\rm H_2} = \frac{N(H_2)}{R} \quad (5)$$

where R is the core diameter and is calculated using $R = \sqrt{a \cdot b}$, a and b being the major and minor axes of the FWHM obtained with ClumpFind and converted to linear distances assuming the source distances of Kim et al. (2020). The mean density of the cores ranges from 0.7×10^5 cm^{-3} to 40.1×10^5 cm^{-3}, with a median value of 5.4×10^5 cm^{-3}.

The core masses are inferred from the SCUBA-2 850 μm continuum fluxes compiled in Yi et al. (2018):

$$M_{\rm core} = \frac{S_\nu^{'} D^2}{\kappa_\nu B_\nu(T_{\rm dust})} \quad (6)$$

where $S_\nu^{'}$ is the flux density of cores from the SCUBA-2 850 μm observations, and D is the distance adopted by Kim et al. (2020). The dust opacity κ_ν is adopted from Beckwith et al. (1990). As listed in Table 1 and Table 2, the mass of the cores ranges from 0.14 ± 0.04 $M_\odot$ to 11.64 ± 2.18 $M_\odot$, with a median mass of 2.27 $M_\odot$.

The high-resolution ALMA 1.3 mm continuum emission traces the total gas mass of the envelope and disk, $M_{\rm enve+disk}$, for each protostar. $M_{\rm enve+disk}$ can be roughly estimated based on the integrated 1.3 mm continuum flux density under an optically thin assumption, which was already calculated in Dutta et al. (2020). The smallest gas mass of protostars in the whole sample is 0.009 $M_\odot$ and the largest mass is 2.312 $M_\odot$, with a median mass of 0.3 $M_\odot$. First, we estimate the mass of the envelope+disk for individual protostars ($M^*_{\rm enve+disk}$). Second, we estimate the total envelope+disk masses ($M_{\rm enve+disk}$) of all protostars within each core. We then calculate a "compact gas fraction" (CGF) to describe the fraction of gas that has accumulated from the dense core into the protostellar envelope and disk:

$${\rm CGF} = M_{\rm enve+disk}/M_{\rm core}. \quad (7)$$

The CGF is a ratio calculated after collecting all the $M_{\rm enve+disk}$ in each core. The CGF is shown in Column (14) of Tables 1 and 2. The minimum and maximum values of the CGF for whole cores are 0.2% and 80%, and the median value is 11%.

Once the perturbations caused by self-gravity inside a molecular cloud are larger than the Jeans length, they can lead

Table 4
Comparison of Physical Parameters of Cores

Parameter	Core(Single system)				Core(Binary/Multiple system)				KS-test	
	Number	Mean	Median	sigma	Number	Mean	Median	sigma	statistic	p-value
$N(H_2)(\times 10^{23}$ cm$^{-2})$	28	2.76	1.90	2.69	13	5.06	4.50	3.52	0.45	4.3%
$n_{H\ 2}(\times 10^5$ cm$^{-3})$	28	8.33	3.70	9.19	13	13.31	7.60	10.64	0.41	7.0%
$\mathcal{M}$	24	1.06	1.00	0.34	12	1.51	1.50	0.43	0.50	3.0%
$L_{jeans}(10^{-2}$ pc)	27	3.95	3.97	1.98	13	3.16	2.86	2.11	0.36	15.0%
$M_{core}(M_\odot)$	28	2.27	1.84	2.39	13	3.67	2.65	3.08	0.31	28.0%
$M_{enve+disk}(M_\odot)$	28	0.30	0.15	0.47	13	0.47	0.29	0.58	0.35	18.9%
$M^*_{\rm enve+disk}(M_\odot)$	28	0.30	0.15	0.47	34	0.18	0.11	0.38	0.22	40.1%
$Size(\times 10^{-1}$ pc)	28	1.02	1.00	0.60	13	1.02	0.90	0.45	0.22	89.7%
Velocity Gradient (km/s)	11	3.93	3.60	1.55	5	4.05	3.62	1.70	0.25	92.6%

Note. G208.68-19.20N2 is not included in the statistics because it is a protobinary system candidate.

the region to become unstable. Hence, Jeans fragmentation may lead to substructures that become binary/multiple systems. The Jeans lengths of dense cores can be calculated via the following equations from Wang et al. (2014):

$$L_{\rm Jeans} = c_s\left(\frac{\pi}{G\rho}\right)^{1/2} = 0.066\left(\frac{T}{10\ {\rm K}}\right)^{1/2}\left(\frac{n}{10^5\ {\rm cm}^{-3}}\right)^{-1/2}{\rm pc} \quad (8)$$

where T is the dust temperature of the dense core from Kounkel et al. (2017), and n is the mean column density of H_2 from Yi et al. (2018). The Jeans lengths of dense cores in our sample range from 2500 au to 19,300 au with a median value of 7000 au.

The Mach number ($\mathcal{M}$) is a measurement of turbulence within dense cores. We adopt the Mach numbers from Kim et al. (2020), which are calculated using

$$\mathcal{M} = \frac{\sigma_{\rm NT}}{c_s} \quad (9)$$

where $\sigma_{\rm NT}$ is the nonthermal velocity dispersion derived from $\sigma_{\rm NT} = \sqrt{\frac{\triangle v}{8\ln 2} - \frac{k_{\rm B}T_k}{m}}$. Here, $k_{\rm B}$ is the Boltzmann constant, T_k the kinetic temperature, $\triangle v$ the $N_2H^+(J=1\text{–}0)$ line width (FWHM), m the mass of the N_2H^+ molecule, and c_s the sound speed, which depends on the temperature assumed. The Mach number of the cores ranges from 0.6 ± 0.1 to 2.4 ± 0.2, with a median value of 1.1.

In order to examine whether the statistical properties of groups of dense cores harboring different types of protostellar systems differ from one another, we calculate the median and mean values of the above-derived core parameters in the two groups of cores, and list them in Table 4. Statistically, the $N(H_2)$, $n(H_2)$, $\mathcal{M}$, and $M_{\rm core}$ of cores containing binary/multiple systems are higher than those of cores forming single stars. The $L_{\rm Jeans}$ and $M^*_{\rm enve+disk}$ of individual protostars in those multiple systems are smaller than those of single systems. The core sizes of the two groups, however, do not show any noticeable difference.

We present the cumulative distribution functions of the core parameters of the two groups of cores in Figure 3. In addition, we use the Kolmogorov–Smirnov (KS) test to gauge whether these two groups of cores have the same underlying core parameter distributions. Overall, the distributions of number density, H_2 column density and Mach number of the two groups appear to differ substantially with p-values smaller than 10%. In particular, the two groups show significant differences in H_2 column density and Mach number with very low p-values (<5%) in the KS test of their distributions. In contrast, the distributions in $M_{\rm core}$, size, and $M_{\rm enve+disk}$ of the two groups of cores are statistically similar, as indicated by the very high p-values (>28%) in the KS test. We find that the proportion of envelope+disk masses below 1 $M_\odot$ for protostars in binary/multiple systems is larger than that in single systems. We discuss these results more thoroughly in Section 5 below.

4.3. N_2H^+ Maps of 16 Protostellar Cores

There are 16 protostellar cores in ALMASOP that have been mapped in $N_2H^+(J=1\text{–}0)$ line emission with the No:45m telescope (Tatematsu et al. 2021). Among the 16 cores, 5 are forming binary/multiple systems and the other 11 contain single protostars. We note that the fraction of binary/multiple systems in this small sample is similar to that of the whole ALMASOP sample. With these data, we can investigate whether there are significant differences in gas kinematics between the two groups of cores. We fit the hyperfine spectra to all N_2H^+ emission lines with signal-to-noise ratios higher than 3, and finally derive the centroid velocity field maps of these cores. The velocity field maps of dense cores that are forming single systems are shown in Figure 4, while the maps of cores forming binary/multiple systems are shown in Figure 5. Most of the cores show velocity gradients in the N_2H^+ emission maps, no matter how many protostars have formed within them.

To evaluate the gas kinematics quantitatively, we derive local velocity gradients across these maps in steps of 10″. The local velocity gradients are shown as arrows on the velocity field maps. In Table 5, we present the maximum, minimum, mean, and standard deviation of the local velocity gradients in these 16 dense cores. The median velocity gradient of the single-system cores ranges from 1.92 to 7.21 km s^{-1} pc^{-1}, with a mean value of 3.94 km s^{-1} pc^{-1}. For comparison, the median velocity gradient of the binary/multiple cores ranges from 1.90 to 7.08 km s^{-1} pc^{-1}, with a mean value of 4.05 km s^{-1} pc^{-1}. We also list the statistics of the velocity gradients in Table 4. These statistics indicate that there is no significant difference in velocity gradient between the two groups of cores with a p-value in the KS test of 92%. These results, however, need to be tested with a much larger sample of cores from higher angular resolution observations, which may separate more clearly the core kinematics from those of the surroundings. The ALMASOP data, unfortunately, do not have high enough spectral resolution or suitable molecular line tracers for gas kinematics studies on the core scale.

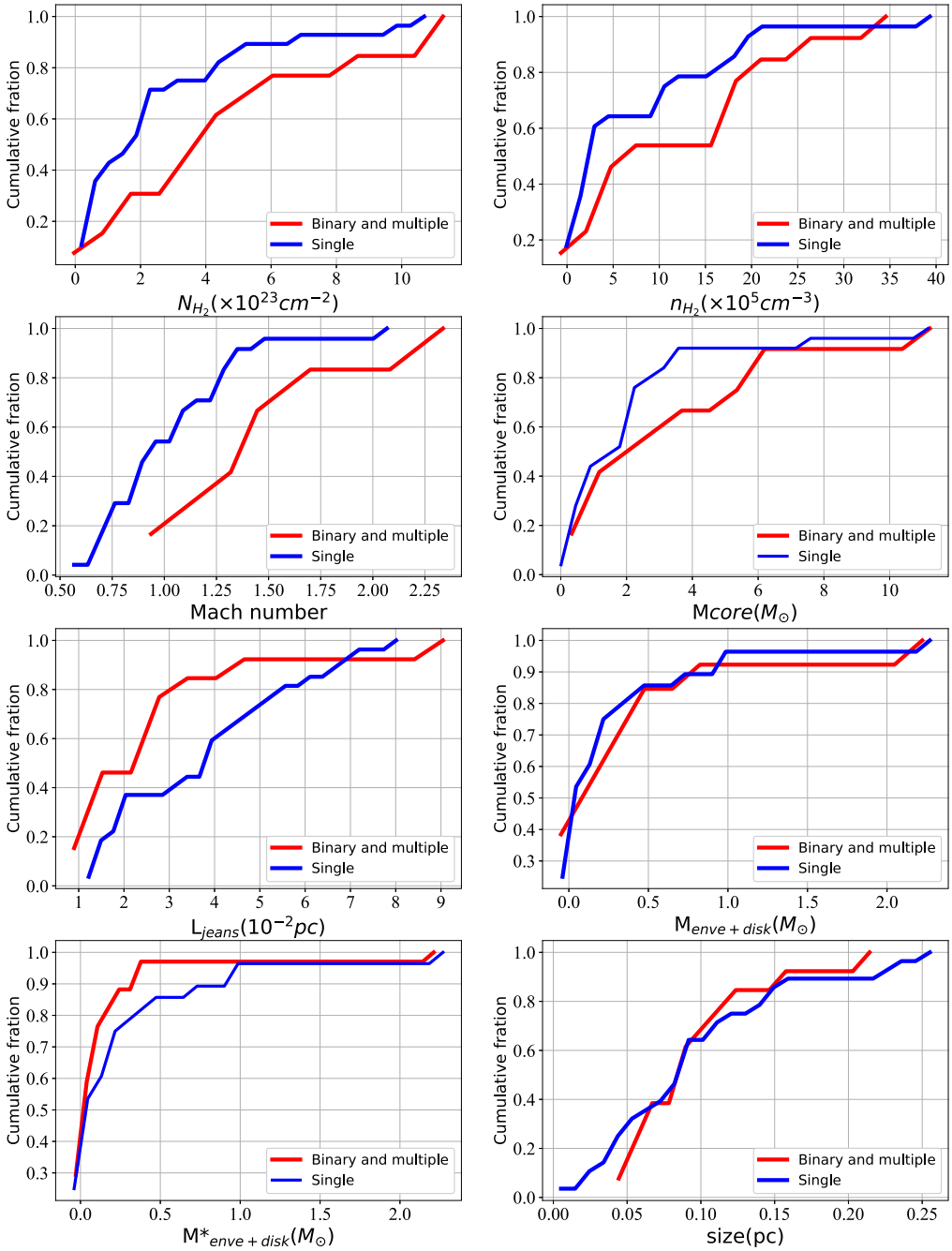

Figure 3. Cumulative distribution functions of the physical parameters in the two groups of dense cores. The compared core parameters are listed in Table 4: H_2 column density, mean density, Mach number, core mass, Jeans length, mass of envelope and disk, and size of core. In each panel, the blue line stands for single-star systems and the red line stands for binary/multiple systems. $M_{\rm enve+disk}$ stands for the total envelope+disk mass of a core. $M^*_{\rm enve+disk}$ stands for each protostar's envelope+disk mass.

4.4. Separation of Protostars in Binary/Multiple Systems

We derive the projected separations among member protostars, for 36 protostars in the 13 binary/multiple-system cores. For high-order systems, we use the MiSTree (minimum spanning tree) package[29] to get the distance or separation between protostars. Figure 6 shows the distribution of separation in the binary/multiple systems. The projected separation between companion protostars of the whole sample ranges from 300 au to 8900 au, and the median projected separation is about 2100 au. Our result highlights a bimodal behavior in the projected separation distribution with one peak around 500 au and another peak around 3500 au, similar in character to the bimodal distribution of projected separations presented in Tobin et al. (2016) and Tobin et al. (2022).

5. Discussion

5.1. Origin of the Multiplicity of Protostars in Dense Cores

In Section 4.2, we statistically compare the physical properties of dense cores that form different systems. We find that dense cores forming binary/multiple systems are

[29] https://joss.theoj.org/papers/10.21105/joss.01721.pdf

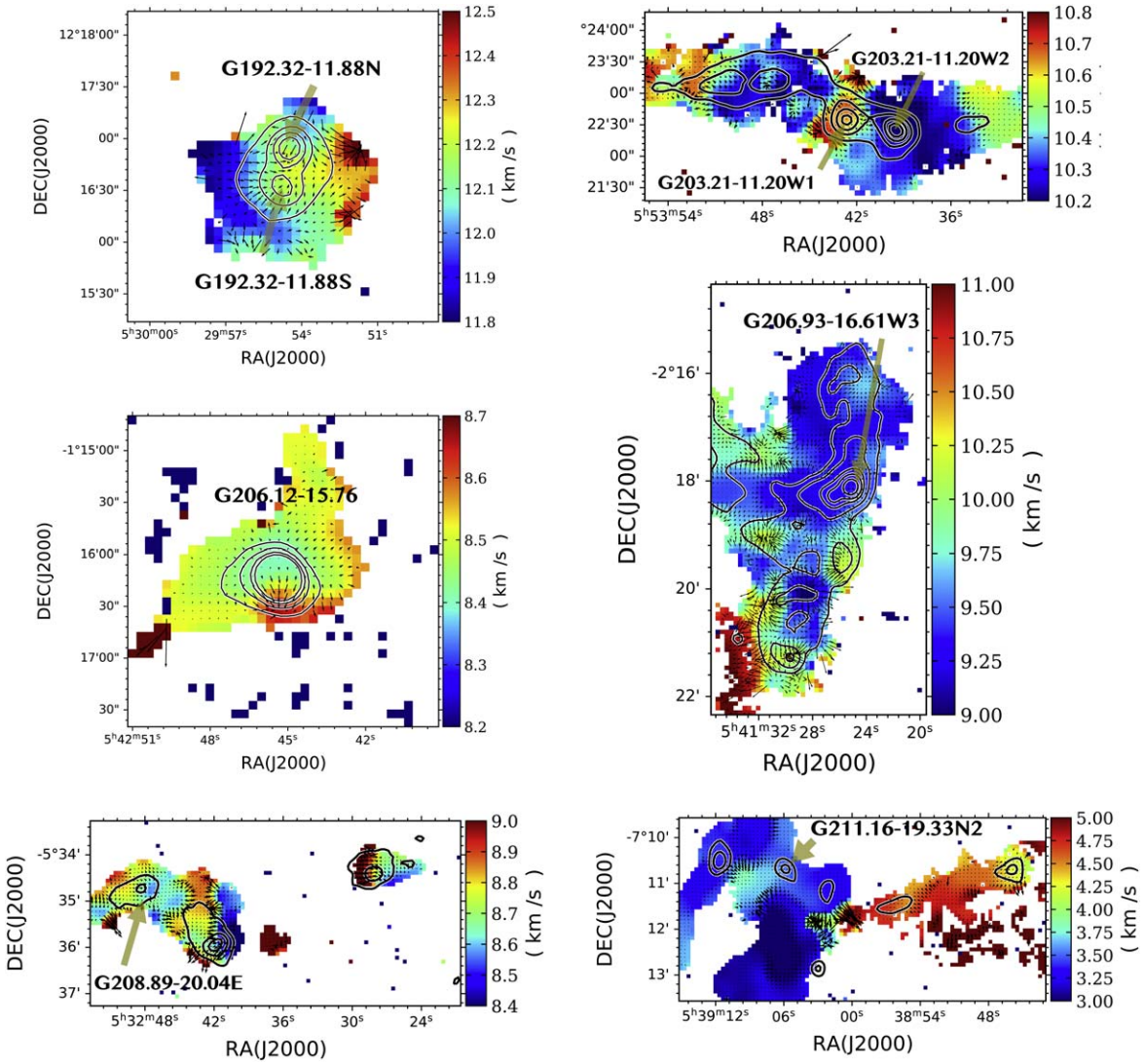

Figure 4. N_2H^+ velocity maps with contours of the JCMT 850 μm data. The contour levels are from 5σ to 25σ with steps of 5σ. The single-system ALMASOP cores are labeled in black. The arrows show the directions of the local velocity gradients, with the lengths indicating their magnitudes.

statistically denser and have higher $N(H_2)$ and n_{H_2} and greater turbulence (higher $\mathcal{M}$) than single-system cores. Dense cores with higher densities also show smaller Jeans lengths, and thus are more likely to fragment into substructures that could form binary/multiple systems.

The higher Mach number of binary/multiple-system cores suggests that turbulent motions are more prevalent in them than in single-system cores. Higher Mach numbers, however, may not reflect the initial turbulence levels before core fragmentation, because outflows from protostars may have injected energy to induce the observed core turbulence (Yun et al. 2021). However, as shown in Figure 9 in the appendix, in most cases, only one protostar in a binary/multiple system drives a highly collimated and energetic bipolar outflow. In addition, outflow properties (e.g., outflow velocities, masses, momenta, and energies) are not significantly different in various dense cores forming either single stars or binary/multiple systems (see S. Dutta et al. 2022, in preparation; Dutta et al. 2020). Therefore, the higher Mach numbers in dense cores forming binary/multiple systems may not be caused by outflow activity.

Furthermore, a higher Mach number may reflect internal core accretion. Statistically, binary/multiple-system cores are more massive than single-system cores while the sizes of the two core groups are indistinguishable. This behavior may indicate that during gravitational collapse, binary/multiple-system cores accumulate more mass through the accretion of gas. The large accretion flows of dense cores may also induce more turbulence inside the cores. However, as shown in Figure 7, Mach numbers are not well correlated with core masses. In general, for dense cores with similar core masses, those cores forming binary/multiple systems have larger Mach numbers than those forming single stars, further suggesting that larger Mach numbers are not associated with larger core masses.

Higher Mach numbers of binary/multiple-system cores could also be related to other bulk motions such as core rotation. Indeed, rotation has been widely revealed in cores of the Orion GMCs (Tatematsu et al. 2016; Xu et al. 2020). In particular, hierarchical protostellar systems may form by rotation-driven fragmentation, as demonstrated in early numerical simulations (Boss 1987, 1991; Chapman et al. 1992; Bonnell et al. 1992; Whitworth et al. 1995). From the single-dish N_2H^+ maps shown in Section 4.3, we do see clear velocity gradients across cores. Whether these velocity gradients are caused by core rotation, however, needs to be tested with

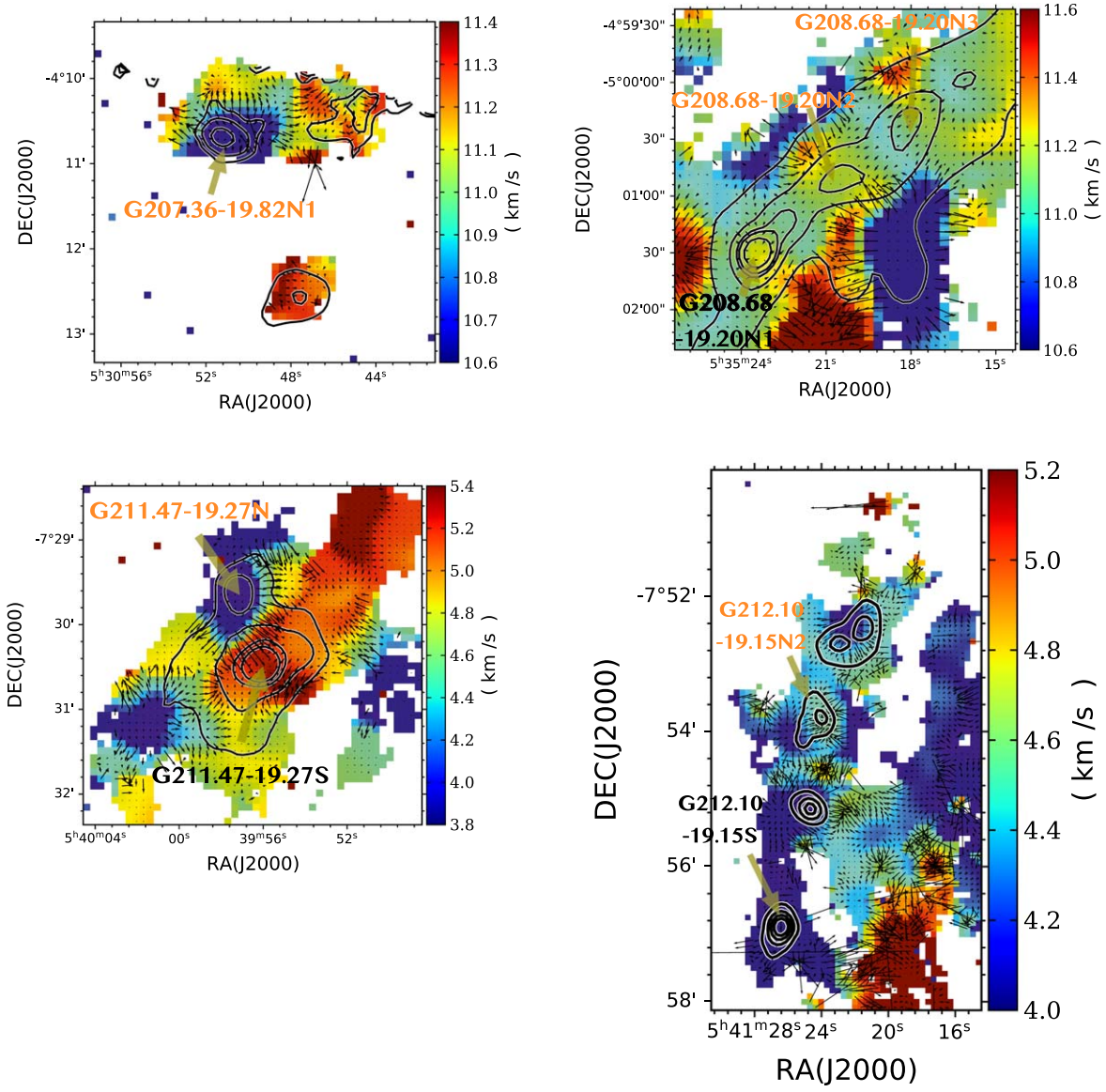

Figure 5. N_2H^+ velocity maps with contours of the JCMT 850 μm data. The contour levels are from 5σ to 25σ with steps of 5σ. The single-system ALMASOP cores are labeled in black and the binary/multiple systems in orange. The arrows show the directions of the local increasing velocity gradients, with the lengths indicating their magnitudes.

higher spatial and spectral resolution observations. Here at least, we find no significant differences in velocity gradients among cores forming various numbers of stars.

Therefore, higher Mach numbers in dense cores likely arise from their initial turbulence levels, and binary/multiple systems tend to form in more turbulent cores. Significant levels of turbulence in cores can be a key trigger of fragmentation because turbulent fluctuations within a bound core can produce multiple nonlinear perturbations in density that exceed the local Jeans mass and cause the overdense region to collapse faster than the background core (Fisher 2004; Goodwin et al. 2004; Offner et al. 2010). In addition, turbulent fragmentation has been suggested to be the dominant channel for binary/multiple-system formation of low-mass stars in numerical simulations (Offner et al. 2010; Tobin et al. 2022).

To summarize, we find that the multiplicity of protostars that form in dense cores may be determined by the core gas density and Mach number. However, correlations between these parameters and time evolution need more refined analyses in the future. We find that protostars are at different evolutionary stages even in the same system, which makes comparison more complicated (for more details on the evolutionary stages, see Section 5.3 below).

5.2. Environmental Effects on the Multiplicity of Protostars

Figure 2 shows the multiplicity of the three GMCs: λ Orionis, Orion B, and Orion A, of which λ Orionis has the lowest MF and CSF. Several previous observations indicated that the physical properties of the three GMCs are markedly diverse. Yi et al. (2018) showed that the mean column densities of dense cores in these clouds can be ranked as λ Orionis, Orion A, and Orion B, from lowest to highest. Furthermore, cores in λ Orionis have the highest dust gas temperatures of the three clouds. Orion A has the most numerous young stars, while Orion B is probably an even younger cloud than Orion A (Bally 2008; Yi et al. 2018). The median core volume density of Orion B is greater than that of Orion A, although

Table 5
Velocity Gradients in Dense Cores

Core Name	Mean ($km\ s^{-1}\ pc^{-1}$)	Median ($km\ s^{-1}\ pc^{-1}$)	Min ($km\ s^{-1}\ pc^{-1}$)	Max ($km\ s^{-1}\ pc^{-1}$)	Std ($km\ s^{-1}\ pc^{-1}$)
(1)	(2)	(3)	(4)	(5)	(6)
G192.32-11.88N	2.49	2.51	0.39	4.14	1.10
G192.32-11.88S	1.87	1.92	1.55	2.33	0.29
G203.21-11.20W1	2.42	2.07	0.48	5.57	1.57
G203.21-11.20W2	3.40	2.75	1.25	7.44	1.67
G206.12-15.76	3.89	4.60	0.22	8.09	2.45
G206.93-16.61W3	4.04	3.60	0.27	10.99	2.53
G208.68-19.20N1	5.14	5.20	1.52	9.80	2.01
G208.89-20.04E	3.36	3.50	0.99	5.23	1.02
G211.16-19.33N2	4.42	4.58	2.82	5.84	0.73
G211.47-19.27S	10.80	7.21	0.13	67.64	12.05
G212.10-19.15S	5.39	5.39	2.02	10.08	2.43
G207.36-19.82N1	8.20	7.08	1.60	16.39	4.41
G208.68-19.20N2	2.12	1.90	0.49	4.67	1.22
G208.68-19.20N3	4.17	4.32	0.63	8.26	1.97
G211.47-19.27N	8.57	3.62	1.02	27.99	8.86
G212.10-19.15N2	3.55	3.32	0.95	8.44	1.69

Note. The eleven cores above the dividing line are those containing only one protostar, and the remaining five are those containing binary/multiple systems.

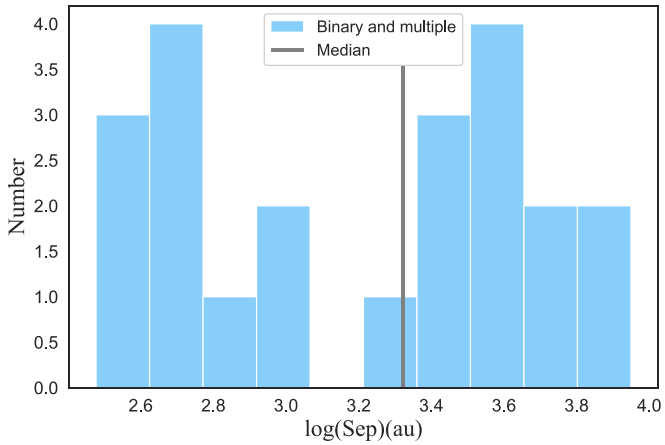

Figure 6. The separations of companion stars are shown as a histogram. The gray vertical line represents the median separation.

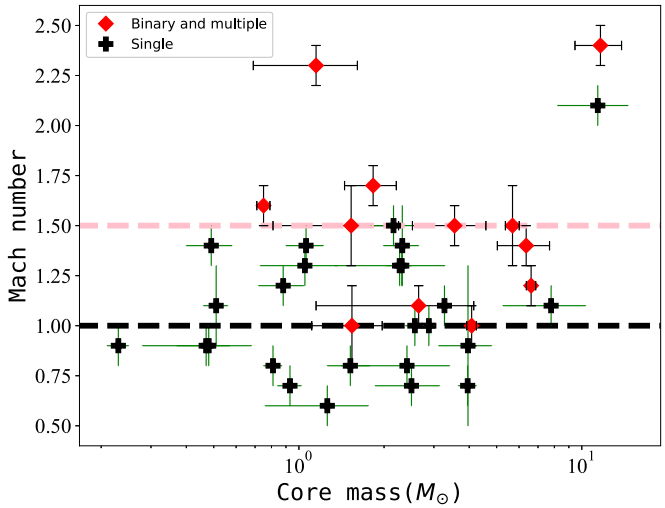

Figure 7. Comparison of core mass and Mach number. The red diamonds represent binary/multiple systems and the black crosses represent single systems. The two dashed lines represent the median Mach numbers of the two core groups.

temperatures are similar in the two subregions (Yi et al. 2018). The higher core volume density reduces the Jeans length in the Orion B cloud, resulting in an overall higher CSF compared to the Orion A cloud. The northern part of Orion A, the ISF, however, stands out in the Orion complex due to its intense star formation (Megeath et al. 2016) and extremely high gas density (Hacar et al. 2018; Schuller et al. 2021; Yun et al. 2021). It is the most massive filament among the Gould Belt clouds (Bally et al. 1987; Schuller et al. 2021). The ISF region, with high-mass star formation in its dense center (the ONC), shows the highest MF and CSF among the Orion GMCs. In contrast, the southern part of Orion A, L1641, containing only low-mass star formation, shows a comparable MF and a smaller CSF when compared with the Orion B GMC. These results indicate that binary/multiple systems form more frequently in high-density clouds.

Meanwhile, the λ Orionis cloud, which has a unique ringlike structure, is composed of an H II region and OB associations in the center. The λ Orionis dense cores that we observed in ALMASOP are exposed to strong UV radiation from the H II region, where the ionization front heats the cores. In addition, the shock and energy input to the environment from supernova explosion feedback and stellar feedback from the OB association, for example, UV radiation and photoevaporation, can influence the star formation process in these bright-rimmed dense cores, consequently limiting the star formation rates therein (Cunha & Smith 1996; Maddalena & Morris 1987; Liu et al. 2016; Kounkel 2020; Yi et al. 2021). In simulations, the radiative feedback of OB stars or H II regions has been shown to be efficient in suppressing fragmentation in dense gas (Myers et al. 2013). However, we note that binary/multiple systems could also form in some dense cores (such as G196.92-10.37 in the B35 cloud) in the λ Orionis GMC because these cores are mostly shielded from the UV radiation due to their high density and large mass. Such cores, however, are very rare

in the λ Orionis GMC (Yi et al. 2018), which may explain the overall low formation rate of binary/multiple stars in the λ Orionis GMC. In contrast, although the ISF region in Orion A is also exposed to strong UV radiation from OB clusters, the ISF shows a very high MF and CSF because of its extremely high density.

5.3. Different Evolutionary Stages of Protostars in Binary/Multiple Systems

The physical properties of protostars in binary/multiple-system cores are discussed in the appendix. We find that the protostars in most multiple systems are not at identical stages of evolution, as judged by their infrared emission. Interestingly, we find that in some systems (such as G196.92-10.37, G205.46-14.56M1, G205.46-14.56S1, G208.68-19.20N2, G208.68-19.20N3, and G210.49-19.79W) infrared-brighter member protostars, which are more evolved, tend to be located farther from the SCUBA-2 core centers than less evolved member protostars. This may indicate that protostars migrate out of their natal cores as they evolve. These wide binary/multiple systems are very likely to become gravitationally unbound as they evolve. Previous statistical studies have also found that the MF and CSF decrease from Class 0 to Class I, and to Class II protostars and field stars (Chen et al. 2013; Tobin et al. 2022), indicating that a large fraction of binary/multiple systems formed in early evolutionary stages will become unbound finally. The ALMASOP data, however, do not have high enough spectral resolution or suitable molecular line tracers for investigating the kinematics and dynamics of member protostars. Therefore, with the present data, we cannot judge whether the binary/multiple systems are gravitationally bound or not. Future more sensitive and higher spectral resolution molecular line observations with ALMA will help determine the gravitational stability or even orbital motions of these systems.

Figure 9 in the appendix presents the CO outflow maps for these systems. In most cases, only one member protostar in a binary/multiple system drives a highly collimated bipolar outflow, which is commonly seen for Class 0 protostars. The other protostars, however, are not associated with energetic outflows, indicating that they could be at a more evolved phase. This difference also implies that protostars in binary/multiple systems could have very different accretion histories or they could have competed for gas to accrete from their natal cores in their formation process.

In the turbulent fragmentation model, multiple protostars can form in the same core with unevenly sized substructures created by turbulent fluctuation. In this scenario, the evolution timescale of each member protostar in the same core could also be very different. Therefore, the turbulent fragmentation model can well explain the different evolutionary stages of member protostars in binary/multiple systems, as witnessed here.

6. Summary

We studied 43 low-mass protostellar cores in the Orion Molecular Cloud Complex that were observed in ALMASOP. We used 1.3 mm continuum emission to detect protostars. We investigated the stellar multiplicity of these cores, and analyzed how the different properties of dense cores may influence the formation of single systems or binary/multiple systems. Our main results are summarized as follows:

(1) From 1.3 mm continuum emission, we identified 13 binary/multiple systems, 1 binary-system candidate, and 29 single-star systems. The overall MF and CSF of the ALMASOP sample in the Orion complex (λ Orionis, Orion B, and Orion A) are $28\% \pm 4\%$ and $51\% \pm 6\%$, respectively. Among the Orion GMCs, λ Orionis has the lowest multiplicity (MF and CSF), while the northern part of Orion A (the ISF) has the highest MF and CSF.

(2) We have determined the separation of companions in each dense core. The median separation is about 2100 au for the 13 binary/multiple systems. A bimodal distribution is seen in companion separation with one peak at ∼500 au and another peak at ∼3500 au.

(3) We found evidence that the properties of the dense core have an effect on binary/multiple-system formation. Specifically, we suggest that the gas density and Mach number of cores may be key factors that promote binary/multiple-star formation in the early stages of dense core to stellar system evolution.

(4) The low multiplicity in λ Orionis may be due to further environmental effects. There, strong UV radiative feedback from the giant H II region may destroy dense cores and suppress the formation of binary/multiple stellar systems.

(5) We found that protostars in each binary/multiple system are usually at very different evolutionary stages. Some protostars drive highly collimated CO outflows and are likely at the Class 0 stage, while other protostars without strong outflows are likely at later stages. More evolved member protostars tend to be located farther from the dense core centers than less evolved member protostars, indicating that protostars migrate out of their natal cores as they evolve.

We note that our studies are limited by the small sample, and also limited by the relatively poor spatial and spectral resolution. Our results could be further tested using future higher spatial and spectral resolution observations toward a more complete dense core sample in various molecular clouds that are in widely different environments.

This paper makes use of the following ALMA data: ADS/JAO.ALMA#2018.1.00302.S. ALMA is a partnership of ESO (representing its member states), NSF (USA) and NINS (Japan), together with NRC (Canada), MOST and ASIAA (Taiwan), and KASI (Republic of Korea), in cooperation with the Republic of Chile. The Joint ALMA Observatory is operated by ESO, auI/NRAO, and NAOJ.

T.L. acknowledges support from the National Natural Science Foundation of China (NSFC) through grants No. 12073061 and No. 12122307, the International Partnership Program of the Chinese Academy of Sciences (CAS) through grant No. 114231KYSB20200009, the Shanghai Pujiang Program (20PJ1415500), and science research grants from the China Manned Space Project with no. CMS-CSST-2021-B06.

K.T. was supported by Japan Society for the Promotion of Science (JSPS) KAKENHI (grant No. 20H05645).

D.J. and J.d.F. are supported by NRC Canada and by NSERC Discovery Grants.

C.-F.L. acknowledge grants from the Ministry of Science and Technology of Taiwan (MoST 107-2119-M-001-040-MY3 and 110-2112-M-001-021-MY3) and Academia Sinica (Investigator Award AS-IA-108-M01).

This research was carried out in part at the Jet Propulsion Laboratory, which is operated by the California Institute of Technology under a contract with the National Aeronautics and Space Administration (80NM0018D0004).

J.-E.L. was supported by a National Research Foundation of Korea grant funded by the Korean government (MSIT) (grant No. 2021R1A2C1011718).

J.H. acknowledges the support of NSFC projects 11873086 and U1631237. This work is sponsored (in part) by the CAS, through a grant to the CAS South America Center for Astronomy in Santiago, Chile.

S.-L.Q. is supported by the NSFC with grant No. 12033005.

S.Z. acknowledges the support of the China Postdoctoral Science Foundation through grant No. 2021M700248.

L.B. gratefully acknowledges support by the ANID BASAL projects ACE210002 and FB210003.

P.S. was supported by a Grant-in-Aid for Scientific Research (KAKENHI No. 18H01259) of JSPS.

V.-M.P. acknowledges support by the grant PID2020-115892GB-I00 funded by MCIN/AEI/10.13039/501100011033.

Facilities: ALMA, JCMT, No:45 m.

Software: astropy (Astropy Collaboration et al. 2013), CASA (McMullin et al. 2007), Starlink (Currie et al. 2014), MiSTree (Naidoo 2019).

Appendix
Description of Individual Binary/Multiple Systems

In this appendix, we provide maps for the 14 dense cores containing binary/multiple systems and discuss the properties of member protostars based on near- and mid-infrared data from Spitzer (3.6 μm, 4.5 μm, and 8 μm) or WISE (3.4 μm, 4.6 μm, and 12 μm) data, JCMT 850 μm data, ALMA 1.3 mm dust continuum data, and CO outflows. Figure 8 shows the infrared and dust continuum images of these systems, and each row of Figure 8 shows one source. Figure 9 presents their CO outflow maps. Table 6 lists the ALMASOP sources that were also observed in the VANDAM survey.

A.1. G196.92-10.37

G196.92-10.37 is located in an isolated dark nebula named B35A (LDN 1594), which is part of the λ Orionis molecular cloud. Several YSOs were found in B35A through the 37 m telescope of the Haystack Observatory and the 43 m telescope of NRAO (Benson & Myers 1989). Connelley et al. (2008) discovered a protobinary system using the UH 2.2 m infrared telescope near the dense core. The Two Micron All Sky Survey (2MASS) and the Spitzer Legacy Program found two YSO candidates, which are identified as protostars B and C in this dense core in our observation (Cutri et al. 2003; Evans et al. 2003; Noble et al. 2013).

As shown in Figure 1(a), G196.92-10.37 is a cometary bright-rimmed core that is forming a small cluster. From the zoomed-in image in Figure 1(b), we find three infrared point sources in the ALMA FOV. The eastern infrared point source is further resolved into a close binary (B and C) in ALMA observations, as shown in Figure 1(c). The southwest infrared point source is also detected in the ALMA 1.3 mm continuum, and is labeled A in Figure 1(c). The infrared point source that is located to the north of A has not been detected in 1.3 mm continuum emission, indicating that it may be a foreground/background star or a very evolved protostar.

The three protostars detected by ALMA are at very different phases of evolution (Dutta et al. 2020). G196.92-10.37_A is a Class 0 source with an envelope+disk mass of 0.069 ± 0.029 $M_{\odot}$. The ALMA 1.3 mm dust continuum observations show an extended structure around this protostar. The G196.92-10.37_B protostar is in the Class I phase, and its envelope+disk mass is 0.042 ± 0.018 $M_{\odot}$. The separation between A and B is ~4700 au. G196.92-10.37_C is a Class I protostar with a low thermal luminosity and an envelope+disk mass of 0.005 ± 0.002 $M_{\odot}$. B and C form a close binary with a projected separation of only ~300 au. The two Class I protostars B and C are located away from the center of the SCUBA-2 core. In contrast, the youngest protostar A is located at the center.

As shown in Figure 9, G196.92-10.37_A drives a strong and large-scale wide-angle outflow, while the outflows detected in the vicinity of G196.92-10.37_B and G196.92-10.37_C are very weak.

A.2. G205.46-14.56M1

G205.46-14.56M1 is located in the L1630 region of Orion B. Many Herbig–Haro objects such as HH 24–26 YSOs have been found near a dense core (Phillips et al. 2001). Among them, HH 24MMS is identified as a binary system driving a bipolar jet discovered by VLA. The 6.9 mm continuum emission reveals that the protostellar system is still in the early phase (Kang et al. 2008). The separation of the companions is about 360 au. In addition, the VISTA/VIRCAM near-infrared survey and JCMT SCUBA-2 survey have found some additional YSOs around the core (Spezzi et al. 2015; Kirk et al. 2016).

Figure 8 presents maps for G205.46-14.56M1. Two protostars (A and B) are identified in our ALMA observation, as shown in panel (c). G205.46-14.56M1_B, located at the center of the SCUBA-2 core, is not detected at infrared wavelengths, indicating that it is a prestellar core or in an extremely early stage of evolution. As shown in Figure 9, this object is not associated with an apparent outflow, further suggesting that it is more likely a prestellar core. Its total gas mass is 2.245 ± 0.960 $M_{\odot}$. G205.46-14.56M1_A is a Class I protostar with an envelope+disk mass of 0.064 ± 0.028 $M_{\odot}$. It is near the edge of the SCUBA-2 core. However, it still drives a very collimated outflow as shown in Figure 8. The distance between these two objects is ~2300 au.

A.3. G205.46-14.56M2

G205.46-14.56M2 is also located in the L1630 region of Orion B. Some YSOs have been previously identified by 2MASS, Spitzer, and JCMT SCUBA surveys (Cutri et al. 2003; Megeath et al. 2012; Kirk et al. 2016). This dense core is surrounded by a well-known HH 24 complex and two Class 0 protostars SSV63E and SSV63W (Ozawa et al. 1999).

In G205.46-14.56M2, we find a rare multiple system containing five protostars. Among them, A/B and C/D seem to form a pair of twin binary systems. From the ALMA 1.3 mm dust continuum image, it seems that the four protostars are not connected to protostar E, as shown in Figure 8(c). G205.46-14.56M2_A and G205.46-14.56M2_B are the closest companions of all, with a separation of only ~700 au. These two protostars are in different evolutionary stages (unclassified phase and Class I phase) with envelope+disk masses of 0.037 ± 0.016 $M_{\odot}$ and 0.124 ± 0.053 $M_{\odot}$, respectively.

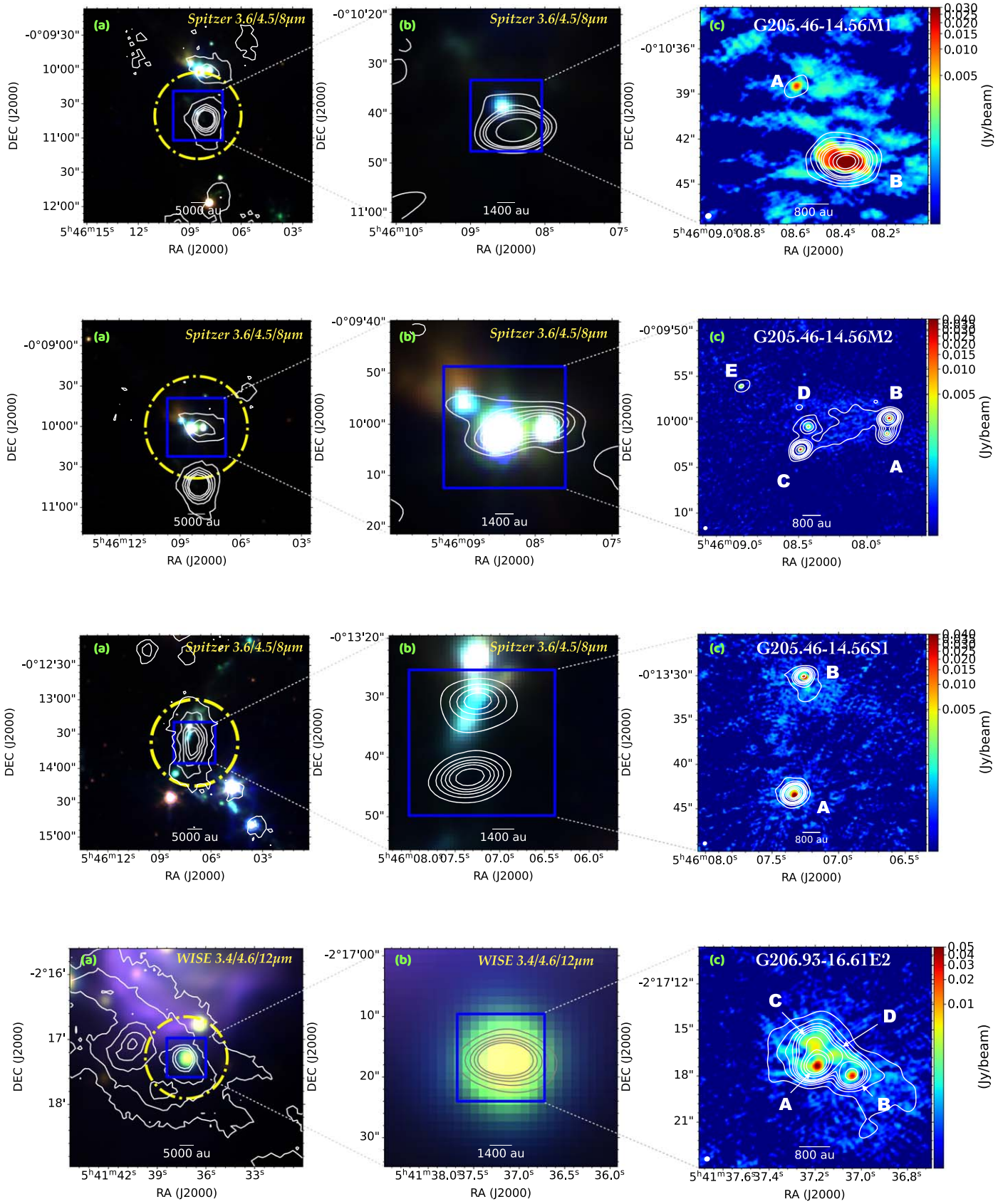

Figure 8. Same as Figure 1 but for other sources. Each row presents maps for one source, and the source name is labeled in panel (c).

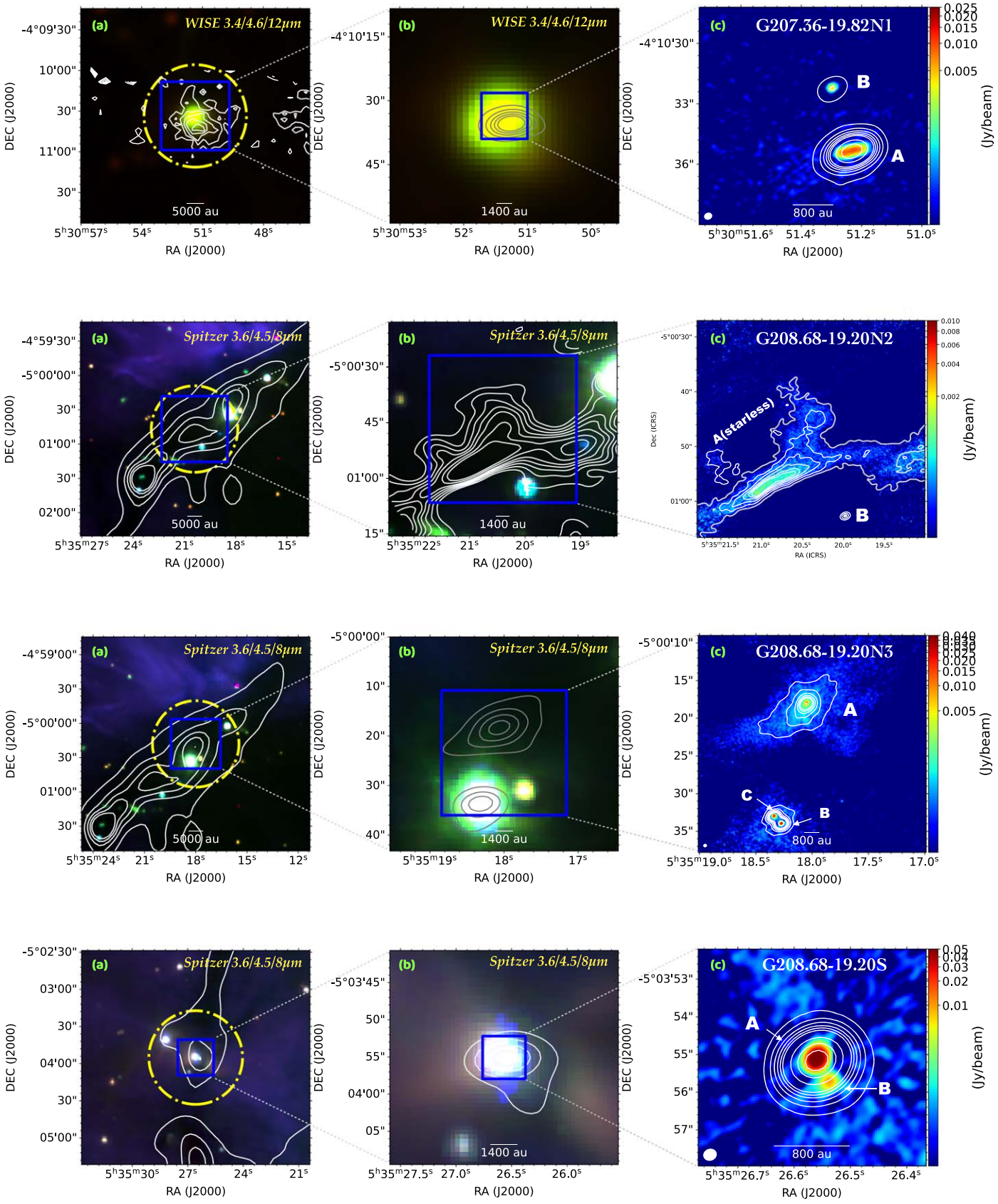

Figure 8. (Continued.)

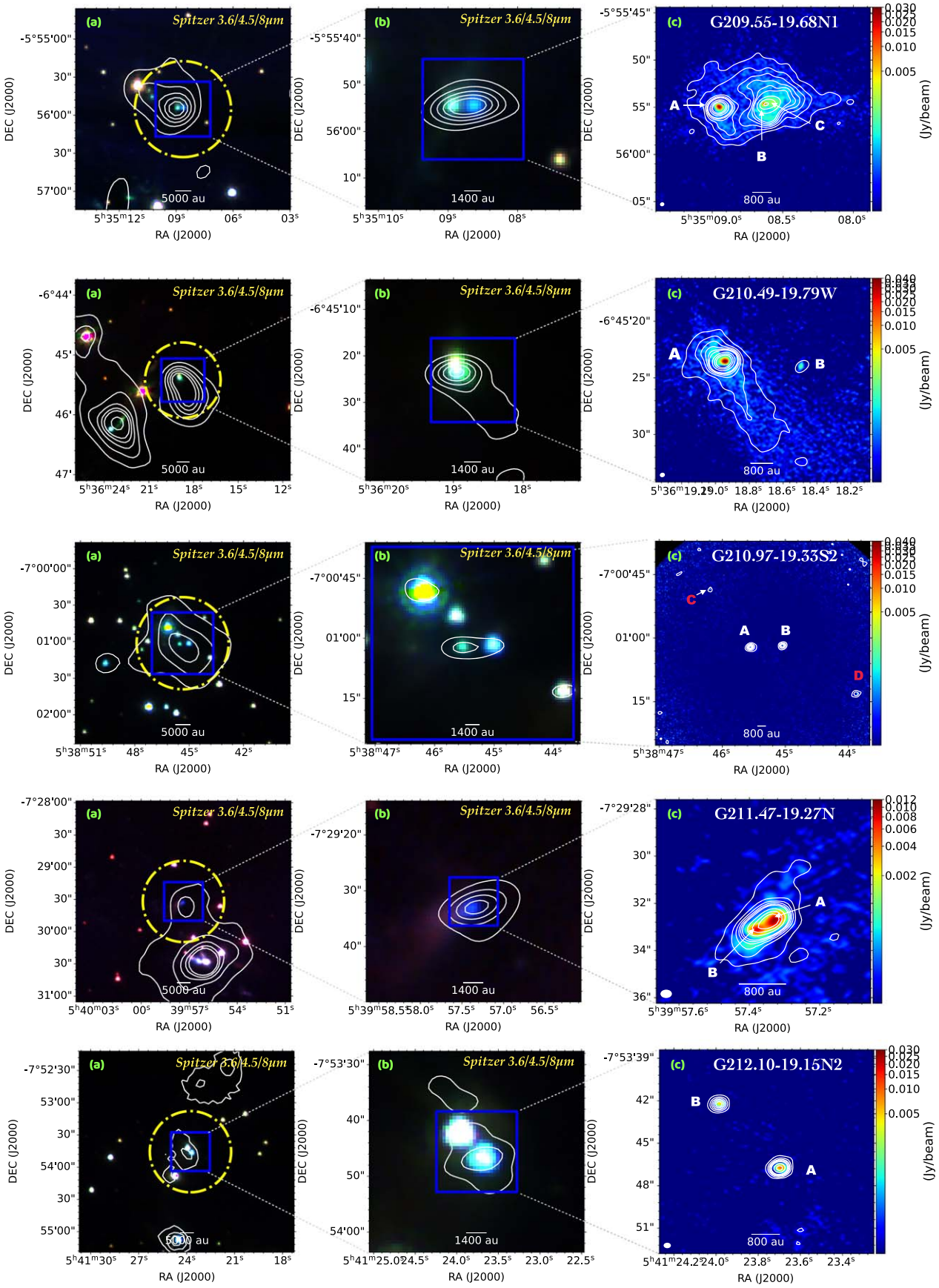

Figure 8. (Continued.)

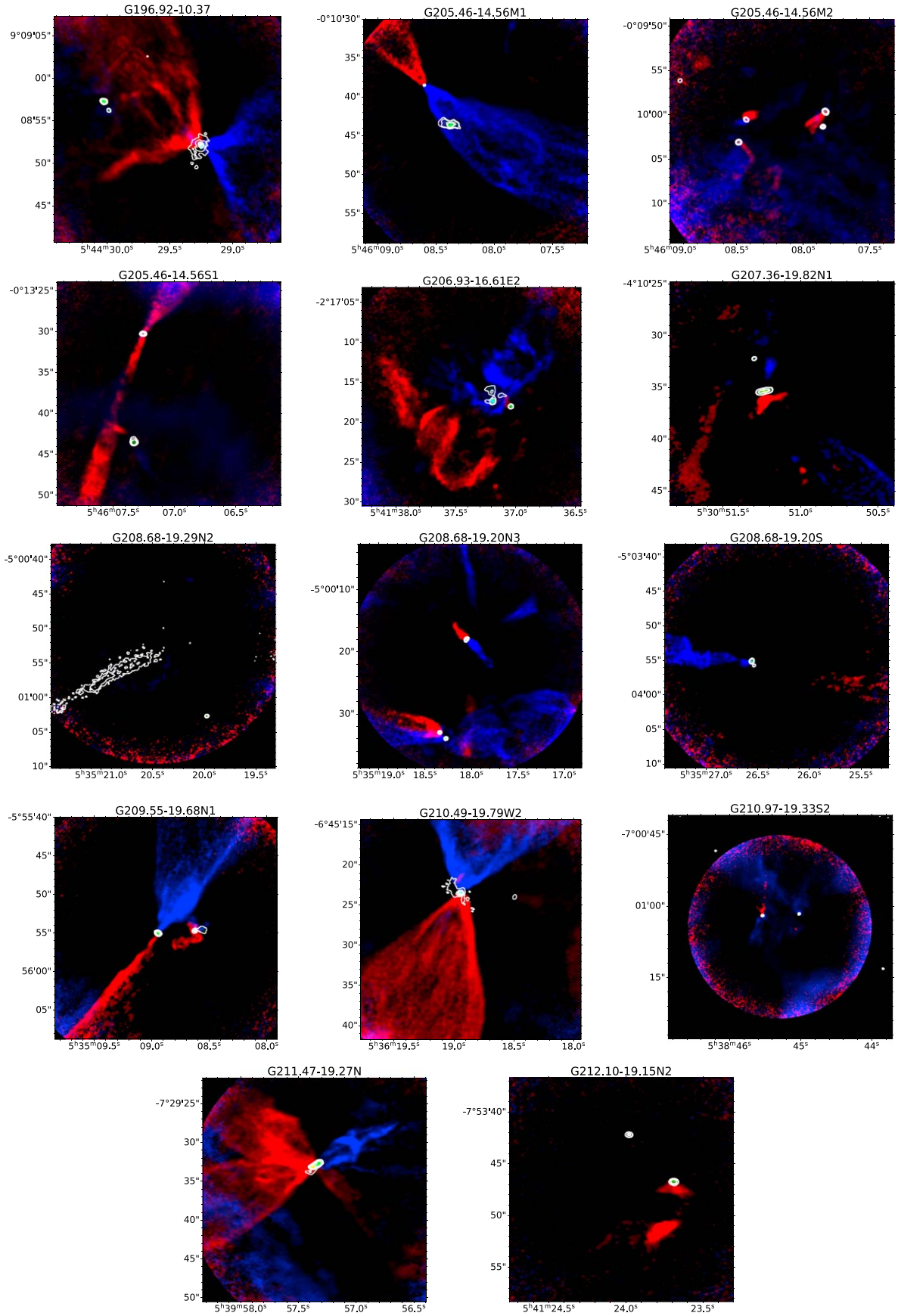

Figure 9. CO outflows.

Table 6
ALMASOP Sources Observed in the VANDAM Survey

ALMASOP Sources (1)	HOPS (2)	Class of HOPS (3)
Binary/Multiple Systems		
G205.46-14.56M1_A	HOPS-317-A	0
G205.46-14.56M1_B	HOPS-317-B	0
G205.46-14.56M2_A	HOPS-387-B	I
G205.46-14.56M2_B	HOPS-387-A	I
G205.46-14.56M2_C	HOPS-386-A	I
G205.46-14.56M2_D	HOPS-386-B	I
G205.46-14.56M2_E	HOPS-386-C	I
G205.46-14.56S1_A	HOPS-358-A	0
G205.46-14.56S1_B	HOPS-358-B	0
G206.93-16.61E2_A	HOPS-298-A	I
G206.93-16.61E2_B	HOPS-298-B	I
G208.68-19.20N2_B	HOPS-89	Flat
G208.68-19.20N3_B	HOPS-92-A-A	Flat
G208.68-19.20N3_C	HOPS-92-B	Flat
G208.68-19.20S_A	HOPS-84-A	I
G208.68-19.20S_B	HOPS-84-B	I
G209.55-19.68N1_B	HOPS-12-B-A	0
G209.55-19.68N1_C	HOPS-12-A	0
G210.49-19.79W_A	HOPS-168-A	0
G210.97-19.33S2_A	HOPS-377	0
G210.97-19.33S2_B	HOPS-144	I
G211.47-19.27N_A	HOPS-290-B	0
G211.47-19.27N_B	HOPS-290-A	0
G212.10-19.15N2_A	HOPS-263	I
G212.10-19.15N2_B	HOPS-262	Flat
Single-star Systems		
G205.46-14.56N1	HOPS-402	0
G205.46-14.56N2	HOPS-401	0
G205.46-14.56S2	HOPS-385	Flat
G205.46-14.56S3	HOPS-315	I
G206.12-15.76*	HOPS-400-B	0
G206.93-16.61W2	HOPS-399	0
G209.55-19.68S1	HOPS-11	0
G209.55-19.68S2	HOPS-10	0
G210.37-19.53S	HOPS-164	0
G210.83-19.47S	HOPS-156	I
G211.01-19.54N	HOPS-153	0
G211.01-19.54S	HOPS-152	0
G211.16-19.33N2	HOPS-133	I
G211.47-19.27S*	HOPS-288-A-A	0
G212.10-19.15S	HOPS-247	0
G212.84-19.45N	HOPS-244	0

Note. The two sources marked with * are identified in the VANDAM survey as binary/multiple systems. HOPS-400 contains two protostars, A and B, separated by 180 au. HOPS-288 contains three protostars; the remaining two protostars are 60 au and 250 au away from HOPS-288-A-A.

G205.46-14.56M2_C and G205.46-14.56M2_D are relatively close, and their separation is ∼1000 au. Their envelope+disk masses are 0.091 ± 0.039 $M_{\odot}$ and 0.028 ± 0.012 $M_{\odot}$. G205.46-14.56M2_D of the two protostars is certified to be in the Class I phase. The distance between these two pairs is ∼3800 au. In our analysis, we find that G205.46-14.56M2_E, located ∼5000 au away from the other four protostars, has an unknown evolutionary stage with an envelope+disk mass of 0.011 ± 0.005 $M_{\odot}$.

As shown in Figure 9, G205.46-14.56M2_B and G205.46-14.56M2_D drive weak but well-collimated outflows. G205.46-14.56M2_A and G205.46-14.56M2_C are also associated with weak outflows.

This multiple system will be discussed in a detailed paper by T. Liu et al. (2022, in preparation).

A.4. G205.46-14.56S1

G205.46-14.56S1 is located in the HH 24–26 region of Orion B. HH 25MMS, a Class 0 source studied extensively by the JCMT, VLA, and IRAM, is situated near this dense core (Gibb & Davis 1998; Bontemps et al. 1995; Lis et al. 1999; Phillips et al. 2001; Gibb et al. 2004; Chen et al. 2013). In addition, several YSOs were discovered in the vicinity by Spitzer, AKARI, and JCMT SCUBA surveys (Megeath et al. 2012; Noble et al. 2013; Kang et al. 2015; Furlan et al. 2016; Kirk et al. 2016).

As shown in Figure 8(a), no infrared sources are found at the center of the 850 μm continuum emission map. Two protostars, however, are identified in our ALMA observation. G205.46-14.56S1_A and G205.46-14.56S1_B are in the Class 0 phase with a separation of ∼5200 au and their envelope+disk masses are 0.151 ± 0.065 $M_{\odot}$ and 0.391 ± 0.167 $M_{\odot}$, respectively.

Figure 9 shows a very collimated outflow traced by ^{12}CO that is driven by G205.46-14.56S1_B. On the other hand, G205.46-14.56S1_A drives a much weaker outflow, which seems to overlay the outflow from G205.46-14.56S1_B.

A.5. G206.93-16.61E2

G206.93-16.61E2 in Orion B is found close to the reflection nebula NGC 2023. Several YSOs have been discovered in JCMT SCUBA-2, Spitzer, and 2MASS all-sky surveys near G206.93-16.61E2 (Cutri et al. 2003; Megeath et al. 2012; Kirk et al. 2016).

As shown in Figure 8(a), a bright infrared source is detected in the ALMA FOV. In the ALMA image, as shown in Figure 8(c), the infrared source is resolved into four protostars in this system. Since these four protostars cannot be separated in the infrared band, their evolutionary stages are not well determined. Their envelope+disk masses are 0.280 ± 0.120 $M_{\odot}$, 0.112 ± 0.048 $M_{\odot}$, 0.219 ± 0.097 $M_{\odot}$, and 0.252 ± 0.110 $M_{\odot}$. Three protostars (A, C, and D) are close to one another with an average separation of ∼450 au, while the other protostar G206.93-16.61E2_B is approximately 1000 au away from them. From Figure 9, one can see that the outflows of this core are very complicated, which seems to be caused by the orbital rotation of the member protostars in the multiple system. More details of this system will be presented in a following paper (Q. Luo et al. 2022, in preparation).

A.6. G207.36-19.82N1

G207.36-19.82N1 is located in Orion A. In the VISTA Orion A survey, a protostar candidate named 2MASS J05305129-0410322 was identified, which we regard as G207.36-19.82N1_B in our ALMA data observation (Meingast et al. 2018). An HH 58 object was also discovered near the core (Tatematsu et al. 2017).

Figure 8(a) shows an infrared source slightly offset from the center of the 850 μm continuum, implying that the evolutionary stage of G207.36-19.82N1_B may be similar to that of G207.36-19.82N1_A. In our ALMA observation, we find a binary system in this dense core. The two protostars have envelope+disk masses of 0.113 ± 0.048 $M_{\odot}$ and

$0.011 \pm 0.005\ M_{\odot}$ and the separation between them is ~5400 au. As shown in Figure 8(c), G207.36-19.82N1_A shows a flattened disklike structure.

Figure 9 reveals a high-velocity outflow with asymmetric structures in the vicinity of G207.36-19.82N1_A, while G207.36-19.82N1_B is not associated with an outflow. Both of them are likely at the Class II phase or an even later phase.

A.7. G208.68-19.20N2

G208.68-19.20N2 is located in Orion A and some YSOs were discovered to be associated with it in JCMT SCUBA and Green Bank Telescope 3.3 mm continuum emission observations (Di Francesco et al. 2008; Schnee et al. 2014).

A protobinary system candidate containing a starless core and a protostar is found in this dense core based on our ALMA 1.3 mm dust continuum observations. The starless core G208.68-19.20N2_A is very dense and will collapse to form a new protostar (Sahu et al. 2021b). The protostar G208.68-19.20N2_B is not associated with an outflow, indicating that it is likely an evolved Class I protostar. The envelope+disk mass of this protostar is just $0.009 \pm 0.001\ M_{\odot}$.

A.8. G208.68-19.20N3

G208.68-19.20N3 is located in a filament in Orion A. As shown in Figure 8(b), our ACA 1.3 mm continuum observations resolve the core into two subcores. The southern subcore is associated with an infrared object, which is further resolved into a close binary in our high-resolution ALMA observations shown in Figure 8(c). In total, the ALMA 1.3 mm emission continuum reveals three protostars in this core. G208.68-19.20N3_A is a Class 0 protostar and its distance from the other two protostars is ~6000 au. G208.68-19.20N3_B and G208.68-19.20N3_C are only ~600 au apart. Both of them are Class I protostars, and are located offset from the center of the SCUBA-2 core. These three protostars have envelope+disk masses of $0.436 \pm 0.189\ M_{\odot}$, $0.078 \pm 0.033\ M_{\odot}$, and $0.093 \pm 0.040\ M_{\odot}$, respectively. Figure 9 shows a collimated outflow from G208.68-19.20N3_A that is perpendicular to its extended disklike structure. The two remaining protostars are also associated with outflows but most of their outflows are located beyond our FOV.

A.9. G208.68-19.20S

G208.68-19.20S is in Orion A, and several protostars have been discovered there in the AzTEC 1.1 mm survey (Shimajiri et al. 2015).

As shown in Figure 8(c), two Class I protostars are found in our ALMA observations, and they are close to each other with a separation of only ~300 au. Their envelope+disk masses are $0.421 \pm 0.180\ M_{\odot}$ for protostar A and $0.043 \pm 0.061\ M_{\odot}$ for protostar B. As shown in Figure 9, the binary system drives an outflow along the east–west direction and the outflow is much weaker than other Class 0 outflows in the ALMASOP sample. Moreover, there is no obvious redshift emission of the high-speed component of ^{12}CO around the protostars.

A.10. G209.55-19.68N1

G209.55-19.68N1 is in Orion A, and a young star named HOPS-12 has been discovered near this dense core (Furlan et al. 2016).

From ALMA data, three protostars are detected in this dense core. Figure 8(c) shows two substructures encasing the three protostars. G209.55-19.68N1_B and G209.55-19.68N1_C reside in the same substructure and are about 400 au apart. G209.55-19.68N1_A lies in another substructure and is separated from G209.55-19.68N1_B by ~4800 au. Their envelope+disk masses are $0.141 \pm 0.060\ M_{\odot}$, $0.061 \pm 0.027\ M_{\odot}$, and $0.132 \pm 0.057\ M_{\odot}$ for components A, B, and C, respectively.

As shown in Figure 9, G209.55-19.68N1_A drives a very collimated outflow. The red lobe of outflow from G209.55-19.68N1_B, however, is distinctly distorted. Moreover, the CO emission near G209.55-19.68N1_C is weak and may be contaminated by the outflow from G209.55-19.68N1_B.

A.11. G210.49-19.79W

G210.49-19.79W is in Orion A. In the vicinity of the dense core, past VLA observations have detected the VLA 4 source with an H_2O maser (Rodríguez et al. 2000).

There are two protostars in different evolutionary stages in the dense core. G210.49-19.79W_A is proved to be in Class 0 and its envelope+disk mass is $0.201 \pm 0.086\ M_{\odot}$. G210.49-19.79W_B is at a more evolved stage and its envelope+disk mass is $0.008 \pm 0.003\ M_{\odot}$. The separation of one from the other is ~2800 au. The younger protostar G210.49-19.79W_A is located at the center of the SCUBA-2 core, while the older protostar is clearly offset from the core center.

As shown in Figure 9, G210.49-19.79W_A drives a collimated wide-angle outflow. We do not detect ^{12}CO emission in the surroundings of G210.49-19.79W_B, which may imply that G210.49-19.79W_B has stopped accretion.

A.12. G210.97-19.33S2

G210.97-19.33S2 is located in Orion A, and we have identified a protobinary system in its center. Its envelope+disk masses are $0.020 \pm 0.009\ M_{\odot}$ and $0.018 \pm 0.008\ M_{\odot}$. The separation between the two protostars (A and B) is ~3400 au. Furthermore, we have discovered two additional protostars in the outer part of the core: G210.97-19.33S2_C and G210.97-19.33S2_D. Figure 8(c) shows that G210.97-19.33S2_C and G210.97-19.33S2_D are more widely separated from the core center. Their position is near the edge of the FOV, and their emission is weak.

According to the high-velocity ^{12}CO emission map in Figure 9, we have only detected outflows near G210.97-19.33S2_A. The CO emission around G210.97-19.33S2_B is very faint. G210.97-19.33S2_C and G210.97-19.33S2_D do not exhibit any line emission.

A.13. G211.47-19.27N

G211.47-19.27N is a faint SCUBA-2 850 μm source to the north of a star cluster in Orion A. Several YSOs have been found in its surroundings by Spitzer observations and the Bolocam Galactic Plane Survey (Megeath et al. 2012; Merello et al. 2015). The infrared source associated with G211.47-19.27N is very faint and diffuse, as shown in Figures 8(a) and (b). As shown in Figure 8(c), two protostars are identified in the ALMA data, and they share a common envelope. The distance between the two protostars is ~300 au, indicating that they are forming a close binary system. These two protostars are in the Class 0 phase, and their envelope+disk masses are $0.067 \pm 0.030\ M_{\odot}$ and $0.039 \pm 0.019\ M_{\odot}$, respectively.

From Figure 9, we can see that the two Class 0 protostars drive powerful outflows, but it is impossible to identify the outflow-driving source.

A.14. G212.10-19.15N2

G212.10-19.15N2 is in Orion A. Two YSOs were detected in this core in Spitzer and 2MASS observations (Cutri et al. 2003; Megeath et al. 2012).

We have identified two Class I protostars in this dense core. G212.10-19.15N2_A has an envelope+disk mass of $0.034 \pm 0.014\ M_{\odot}$, and G212.10-19.15N2_B has an envelope +disk mass of $0.014 \pm 0.006\ M_{\odot}$. They are ~2800 au apart. According to Figure 9, neither of these two protostars exhibits a clear outflow.

ORCID iDs

Qiu-yi Luo (罗秋怡) https://orcid.org/0000-0003-4506-3171
Tie Liu (刘铁) https://orcid.org/0000-0002-5286-2564
Ken'ichi Tatematsu https://orcid.org/0000-0002-8149-8546
Sheng-Yuan Liu https://orcid.org/0000-0003-4603-7119
Pak Shing Li https://orcid.org/0000-0001-8077-7095
James di Francesco https://orcid.org/0000-0002-9289-2450
Doug Johnstone https://orcid.org/0000-0002-6773-459X
Paul F. Goldsmith https://orcid.org/0000-0002-6622-8396
Somnath Dutta https://orcid.org/0000-0002-2338-4583
Naomi Hirano https://orcid.org/0000-0001-9304-7884
Chin-Fei Lee https://orcid.org/0000-0002-3024-5864
Di Li https://orcid.org/0000-0003-3010-7661
Kee-Tae Kim https://orcid.org/0000-0003-2412-7092
Chang Won Lee https://orcid.org/0000-0002-3179-6334
Jeong-Eun Lee https://orcid.org/0000-0003-3119-2087
Mika Juvela https://orcid.org/0000-0002-5809-4834
Jinhua He https://orcid.org/0000-0002-3938-4393
Sheng-Li Qin https://orcid.org/0000-0003-2302-0613
Hong-Li Liu https://orcid.org/0000-0003-3343-9645
David Eden https://orcid.org/0000-0002-5881-3229
Woojin Kwon https://orcid.org/0000-0003-4022-4132
Dipen Sahu https://orcid.org/0000-0002-4393-3463
Shanghuo Li https://orcid.org/0000-0003-1275-5251
Feng-Wei Xu https://orcid.org/0000-0001-5950-1932
Shih-Ying Hsu https://orcid.org/0000-0002-1369-1563
Leonardo Bronfman https://orcid.org/0000-0002-9574-8454
Patricio Sanhueza https://orcid.org/0000-0002-7125-7685
Veli-Matti Pelkonen https://orcid.org/0000-0002-8898-1047
Yue-fang Wu https://orcid.org/0000-0002-5076-7520
Xiao-feng Mai https://orcid.org/0000-0001-7573-0145
Edith Falgarone https://orcid.org/0000-0003-0693-2477
Zhi-Qiang Shen https://orcid.org/0000-0003-3540-8746

References

Adams, F. C., Ruden, S. P., & Shu, F. H. 1989, ApJ, 347, 959
Astropy Collaboration, Robitaille, T. P., Tollerud, E. J., et al. 2013, A&A, 558, A33
Bally, J. 2008, in Handbook of Star Forming Regions, Volume I: The Northern Sky, ed. B. Reipurth (San Francisco, CA: ASP), 459
Bally, J., Langer, W. D., Stark, A. A., & Wilson, R. W. 1987, ApJL, 312, L45
Beckwith, S. V. W., Sargent, A. I., Chini, R. S., & Guesten, R. 1990, AJ, 99, 924
Beichman, C. A., Myers, P. C., Emerson, J. P., et al. 1986, ApJ, 307, 337
Benson, P. J., & Myers, P. C. 1989, ApJS, 71, 89
Bergin, E. A., & Tafalla, M. 2007, ARA&A, 45, 339
Bonnell, I., Arcoragi, J.-P., Martel, H., & Bastien, P. 1992, ApJ, 400, 579
Bonnell, I. A., & Bate, M. R. 1994, MNRAS, 269, L45
Bontemps, S., Andre, P., & Ward-Thompson, D. 1995, A&A, 297, 98
Boss, A. P. 1987, ApJ, 319, 149
Boss, A. P. 1991, Natur, 351, 298
Chapman, S., Pongracic, H., Disney, M., et al. 1992, Natur, 359, 207
Chen, X., Arce, H. G., Zhang, Q., et al. 2013, ApJ, 768, 110
Cohen, M., & Kuhi, L. V. 1979, ApJS, 41, 743
Connelley, M. S., Reipurth, B., & Tokunaga, A. T. 2008, AJ, 135, 2526
Connelley, M. S., Reipurth, B., & Tokunaga, A. T. 2009, AJ, 138, 1193
Cunha, K., & Smith, V. V. 1996, A&A, 309, 892
Currie, M. J., Berry, D. S., Jenness, T., et al. 2014, in ASP Conf. Ser. 485, Astronomical Data Analysis Software and Systems XXIII, ed. N. Manset & P. Forshay (San Francisco, CA: ASP), 391
Cutri, R. M., Skrutskie, M. F., van Dyk, S., et al. 2003, yCat, 2246, 0
Daemgen, S., Bonavita, M., Jayawardhana, R., Lafrenière, D., & Janson, M. 2015, ApJ, 799, 155
di Francesco, J., Evans, N. J. I., Caselli, P., et al. 2007, in Protostars and Planets V, ed. B. Reipurth, D. Jewitt, & K. Keil (Tucson, AZ: Univ. Arizona Press), 17
Di Francesco, J., Johnstone, D., Kirk, H., MacKenzie, T., & Ledwosinska, E. 2008, ApJS, 175, 277
Duchêne, G., Bontemps, S., Bouvier, J., et al. 2007, A&A, 476, 229
Duchêne, G., Bouvier, J., Bontemps, S., André, P., & Motte, F. 2004, A&A, 427, 651
Duchêne, G., & Kraus, A. 2013, ARA&A, 51, 269
Duquennoy, A., & Mayor, M. 1991, A&A, 500, 337
Dutta, S., Lee, C.-F., Liu, T., et al. 2020, ApJS, 251, 20
Eden, D. J., Liu, T., Kim, K.-T., et al. 2019, MNRAS, 485, 2895
Evans, N. J. I., Allen, L. E., Blake, G. A., et al. 2003, PASP, 115, 965
Fisher, R. T. 2004, ApJ, 600, 769
Furlan, E., Fischer, W. J., Ali, B., et al. 2016, ApJS, 224, 5
Gibb, A. G., & Davis, C. J. 1998, MNRAS, 298, 644
Gibb, A. G., Richer, J. S., Chandler, C. J., & Davis, C. J. 2004, ApJ, 603, 198
Goodwin, S. P., Whitworth, A. P., & Ward-Thompson, D. 2004, A&A, 423, 169
Hacar, A., Tafalla, M., Forbrich, J., et al. 2018, A&A, 610, A77
Haisch, K. E., Jr., Greene, T. P., Barsony, M., & Stahler, S. W. 2004, AJ, 127, 1747
Hatziminaoglou, E., Farrah, D., Humphreys, E., et al. 2018, MNRAS, 480, 4974
Heggie, D. C. 1975, MNRAS, 173, 729
Hsu, S.-Y., Liu, S.-Y., Liu, T., et al. 2020, ApJ, 898, 107
Hsu, S.-Y., Liu, S.-Y., Liu, T., et al. 2022, ApJ, 927, 218
Juvela, M., Ristorcelli, I., Montier, L. A., et al. 2010, A&A, 518, L93
Kang, M., Choi, M., Ho, P. T. P., & Lee, Y. 2008, ApJ, 683, 267
Kang, M., Choi, M., Stutz, A. M., & Tatematsu, K. 2015, ApJ, 814, 31
Kim, G., Tatematsu, K., Liu, T., et al. 2020, ApJS, 249, 33
Kirk, H., Francesco, J. D., Johnstone, D., et al. 2016, ApJ, 817, 167
Kounkel, M. 2020, ApJ, 902, 122
Kounkel, M., Hartmann, L., Loinard, L., et al. 2017, ApJ, 834, 142
Kounkel, M., Megeath, S. T., Poteet, C. A., Fischer, W. J., & Hartmann, L. 2016, ApJ, 821, 52
Kraus, A. L., & Hillenbrand, L. A. 2007, ApJ, 662, 413
Kraus, A. L., & Hillenbrand, L. A. 2012, ApJ, 757, 141
Kraus, A. L., Ireland, M. J., Martinache, F., & Hillenbrand, L. A. 2011, ApJ, 731, 8
Lee, J.-E., Lee, S., Dunham, M. M., et al. 2017, NatAs, 1, 0172
Lee, K. I., Dunham, M. M., Myers, P. C., et al. 2015, ApJ, 814, 114
Lee, Y.-N., Offner, S. S. R., Hennebelle, P., et al. 2020, SSRv, 216, 70
Lippincott, S. L. 1978, SSRv, 22, 153
Lis, D. C., Menten, K. M., & Zylka, R. 1999, ApJ, 527, 856
Liu, T., Kim, K.-T., Juvela, M., et al. 2018, ApJS, 234, 28
Liu, T., Zhang, Q., Kim, K.-T., et al. 2016, ApJS, 222, 7
Lomax, O., Whitworth, A. P., Hubber, D. A., Stamatellos, D., & Walch, S. 2015, MNRAS, 447, 1550
Ma, J., Cooray, A., Nayyeri, H., et al. 2019, ApJS, 244, 30
Maddalena, R. J., & Morris, M. 1987, ApJ, 323, 179
Marcy, G. W., & Benitz, K. J. 1989, ApJ, 344, 441
McMullin, J. P., Waters, B., Schiebel, D., Young, W., & Golap, K. 2007, in ASP Conf. Ser. 376, Astronomical Data Analysis Software and Systems XVI, ed. R. A. Shaw, F. Hill, & D. J. Bell (San Francisco, CA: ASP), 127
Megeath, S. T., Gutermuth, R., Muzerolle, J., et al. 2012, AJ, 144, 192
Megeath, S. T., Gutermuth, R., Muzerolle, J., et al. 2016, AJ, 151, 5
Meingast, S., Alves, J., & Lombardi, M. 2018, A&A, 614, A65
Merello, M., Evans, N. J. I., Shirley, Y. L., et al. 2015, ApJS, 218, 1

Montillaud, J., Juvela, M., Rivera-Ingraham, A., et al. 2015, A&A, 584, A92
Myers, A. T., McKee, C. F., Cunningham, A. J., Klein, R. I., & Krumholz, M. R. 2013, ApJ, 766, 97
Naidoo, K. 2019, JOSS, 4, 1721
Noble, J. A., Fraser, H. J., Aikawa, Y., Pontoppidan, K. M., & Sakon, I. 2013, ApJ, 775, 85
Offner, S. S. R., Kratter, K. M., Matzner, C. D., Krumholz, M. R., & Klein, R. I. 2010, ApJ, 725, 1485
Ozawa, H., Nagase, F., Ueda, Y., Dotani, T., & Ishida, M. 1999, ApJ, 523, L81
Phillips, R. R., Gibb, A. G., & Little, L. T. 2001, MNRAS, 326, 927
Planck Collaboration, Ade, P. A. R., Aghanim, N., et al. 2011, A&A, 536, A22
Planck Collaboration, Ade, P. A. R., Aghanim, N., et al. 2016, A&A, 594, A28
Raghavan, D., McAlister, H. A., Henry, T. J., et al. 2010, ApJS, 190, 1
Reipurth, B., Clarke, C. J., Boss, A. P., et al. 2014, in Protostars and Planets VI, ed. H. Beuther et al. (Tucson, AZ: Univ. Arizona Press), 267
Reipurth, B., Guimarães, M. M., Connelley, M. S., & Bally, J. 2007, AJ, 134, 2272
Rodríguez, L. F., Delgado-Arellano, V. G., Gómez, Y., et al. 2000, AJ, 119, 882
Sahu, D., Liu, S.-Y., & Liu, T. 2021a, FrASS, 8, 137
Sahu, D., Liu, S.-Y., Liu, T., et al. 2021b, ApJL, 907, L15
Schnee, S., Mason, B., Di Francesco, J., et al. 2014, MNRAS, 444, 2303
Schuller, F., André, P., Shimajiri, Y., et al. 2021, A&A, 651, A36
Shimajiri, Y., Kitamura, Y., Nakamura, F., et al. 2015, ApJS, 217, 7
Shu, F. H., Adams, F. C., & Lizano, S. 1987, ARA&A, 25, 23
Spezzi, L., Petr-Gotzens, M. G., Alcalá, J. M., et al. 2015, A&A, 581, A140
Tatematsu, K., Liu, T., Ohashi, S., et al. 2017, ApJS, 228, 12
Tatematsu, K., Ohashi, S., Sanhueza, P., et al. 2016, PASJ, 68, 24
Tatematsu, K., Kim, G., Liu, T., et al. 2021, ApJS, 256, 25
Tobin, J. J., Kratter, K. M., Persson, M. V., et al. 2016, Natur, 538, 483
Tobin, J. J., Looney, L. W., Li, Z.-Y., et al. 2016, ApJ, 818, 73
Tobin, J. J., Offner, S. S. R., Kratter, K. M., et al. 2022, ApJ, 925, 39
Wang, K., Zhang, Q., Testi, L., et al. 2014, MNRAS, 439, 3275
Whitworth, A. P., Chapman, S. J., Bhattal, A. S., et al. 1995, MNRAS, 277, 727
Wright, E. L., Eisenhardt, P. R. M., Mainzer, A. K., et al. 2010, AJ, 140, 1868
Wu, Y., Liu, T., Meng, F., et al. 2012, ApJ, 756, 76
Xu, F., Wu, Y., Liu, T., et al. 2021, ApJ, 920, 103
Xu, X., Li, D., Dai, Y. S., Fuller, G. A., & Yue, N. 2020, ApJL, 894, L20
Yi, H.-W., Lee, J.-E., Kim, K.-T., et al. 2021, ApJS, 254, 14
Yi, H.-W., Lee, J.-E., Liu, T., et al. 2018, ApJS, 236, 51
Yun, H.-S., Lee, J.-E., Evans, N. J., et al. 2021, ApJ, 921, 31